

Statistics of convective cloud turbulence from a comprehensive turbulence retrieval method for radar observations

Article

Accepted Version

Feist, M. M., Westbrook, C. D., Clark, P. A. ORCID: <https://orcid.org/0000-0003-1001-9226>, Stein, T. H. M. ORCID: <https://orcid.org/0000-0002-9215-5397>, Lean, H. W. and Stirling, A. J. (2019) Statistics of convective cloud turbulence from a comprehensive turbulence retrieval method for radar observations. Quarterly Journal of the Royal Meteorological Society, 145 (719). pp. 727-744. ISSN 1477-870X doi: <https://doi.org/10.1002/qj.3462> Available at <https://centaur.reading.ac.uk/81215/>

It is advisable to refer to the publisher's version if you intend to cite from the work. See [Guidance on citing](#).

To link to this article DOI: <http://dx.doi.org/10.1002/qj.3462>

Publisher: Royal Meteorological Society

All outputs in CentAUR are protected by Intellectual Property Rights law, including copyright law. Copyright and IPR is retained by the creators or other copyright holders. Terms and conditions for use of this material are defined in the [End User Agreement](#).

www.reading.ac.uk/centaur

CentAUR

Central Archive at the University of Reading

Reading's research outputs online

**Statistics of Convective Cloud Turbulence from a Comprehensive Turbulence
Retrieval Method for Radar Observations**

Matthew M. Feist^{a*}, Chris D. Westbrook^a, Peter A. Clark^a, Thorwald HM. Stein^a,
Humphrey W. Lean^b, Alison J. Stirling^c

^a*Department of Meteorology, University of Reading, Reading, UK.*

^b*MetOffice@Reading, University of Reading, Reading, UK.*

^c*Met Office, Exeter, UK.*

**Correspondence to: M. M. Feist, Department of Meteorology, University of Reading, Reading,*

RG6 6BB, UK. E-mail: M.M.Feist@pgr.reading.ac.uk

1 **Turbulent mixing processes are important in determining the evolution of convective clouds,**
2 **and the production of convective precipitation. However, the exact nature of these impacts**
3 **remains uncertain due to limited observations. Model simulations show that assumptions made**
4 **in parametrising turbulence can have a marked effect on the characteristics of simulated**
5 **clouds. This leads to significant uncertainty in forecasts from convection-permitting numerical**
6 **weather prediction (NWP) models. This contribution presents a comprehensive method to**
7 **retrieve turbulence using Doppler weather radar to investigate turbulence in observed clouds.**
8 **This method involves isolating the turbulent component of the Doppler velocity spectrum**
9 **width, expressing turbulence intensity as an eddy dissipation rate, ϵ . By applying this method**
10 **throughout large datasets of observations collected over the southern UK using the (0.28°**
11 **beam-width) Chilbolton Advanced Meteorological Radar (CAMRa), statistics of convective**

12 cloud turbulence are presented. Two contrasting case days are examined: a shallow “shower”
13 case, and a “deep convection” case, exhibiting stronger and deeper updrafts. In our
14 observations, ε generally ranges from $10^{-3} - 10^{-1} \text{ m}^2 \text{ s}^{-3}$, with the largest values found
15 within, around and above convective updrafts. Vertical profiles of ε suggest that turbulence is
16 much stronger in deep convection; 95th percentile values increase with height from $0.03 - 0.1$
17 $\text{m}^2 \text{ s}^{-3}$, compared to approximately constant values of $0.02 - 0.03 \text{ m}^2 \text{ s}^{-3}$ throughout the depth
18 of shower cloud. In updraft regions on both days, the 95th percentile of ε has significant ($p <$
19 10^{-3}) positive correlations with the updraft velocity, and the horizontal shear in the updraft
20 velocity, with weaker positive correlations with updraft dimensions. The ε -retrieval method
21 presented considers a very broad range of conditions, providing a reliable framework for
22 turbulence retrieval using high-resolution Doppler weather radar. In applying this method
23 across many observations, the derived turbulence statistics will form the basis for evaluating
24 the parametrisation of turbulence in NWP models.

25

26 **Keywords:** Radar; Doppler spectrum width; turbulence; convection; eddy dissipation rate; clouds.

27

28 1 Introduction

29 The effects of turbulence on the structure and evolution of convective clouds remain unclear in
30 observations and numerical weather prediction (NWP) models. The turbulent entrainment of dry
31 environmental air into cumulus clouds has long been known to play an important role in their growth
32 and decay (Blyth, 1993). The specific location of entrained air can have a varied and substantial
33 impact on resulting air motions within the cloud (Blyth *et al.*, 1988). Turbulent mixing within clouds
34 significantly impacts the microphysical processes governing the initiation of convective
35 precipitation; the presence of turbulence accelerates cloud drop growth through increased rates of
36 collision and coalescence (Grover and Pruppacher, 1985; Khain and Pinsky, 1995; Vohl *et al.*, 1999;

Observing turbulence in convective clouds

37 Falkovic *et al.*, 2002; Pinsky and Khain, 2002). Although there is much evidence for the effects of
38 turbulence on cloud processes, there remains uncertainty in their precise nature, and the implications
39 for cloud evolution.

40 In recent years, regional numerical weather prediction (NWP) has improved to sufficient
41 resolution that it is worthwhile abandoning the parametrisation of deep convective clouds, and,
42 instead, allowing the unstable growth of explicit convective clouds. However, it is not feasible to
43 forecast using resolutions sufficient to properly resolve all of the important features of the flow.
44 Hence such models are known as 'convection-permitting models' (CPMs, Clark *et al.*, 2016). Physical
45 processes occurring on scales below those resolved in CPMs, such as turbulence, remain
46 parametrised. CPMs generally adopt mixing-length-based turbulence closure schemes from Large-
47 Eddy Simulation (LES) models, such as the Smagorinsky-Lilly sub-grid scheme. It is not often clear
48 whether the assumptions implicit in these schemes (such as the ability of the model to resolve an
49 inertial sub-range of turbulence) are valid for CPMs, especially when using grid-lengths larger than
50 100 m. Model simulations show that the configuration of turbulence parametrisations can have a
51 profound effect on the characteristics of simulated clouds (e.g. Hanley *et al.*, 2015). Until we advance
52 our understanding of the effects of turbulence in observed clouds, justifiable attempts to evaluate and
53 improve these parametrisations are difficult to make.

54 To improve our understanding of turbulence in observed clouds for model evaluation,
55 observations of convective storm turbulence can be made with Doppler weather radar. By isolating
56 the turbulent component to the Doppler velocity spectrum variance, near-instantaneous observations
57 of turbulence can be made across large swathes of atmosphere. Turbulence retrieval with weather
58 radar has clear benefits over using methods such as aircraft or ascent measurements which can only
59 collect time-series information from single points in space. Radar retrieved fields of turbulence,
60 expressed for convenience in terms of the dissipation rate of turbulent kinetic energy, ϵ , can be used
61 to investigate relationships with storm strength and structure in a statistical sense for model
62 evaluation.

Observing turbulence in convective clouds

63 The accuracy to which ε can be derived using the Doppler variance method is dependent on the
64 accurate removal of variances associated with processes aside from inertial sub-range turbulence.
65 Due to this somewhat indirect approach, evaluation of the Doppler variance method has previously
66 been necessary through comparison of ε estimates with in situ measurements and other radar retrieval
67 techniques. Using Doppler weather radar, Labitt (1981) and Meischner *et al.* (2001) demonstrated
68 good agreement between ε derived from the Doppler variance method when compared with co-
69 ordinated aircraft measurements in convective storms. Brewster and Zrnich (1986) found a high level
70 of agreement between ε from Doppler variance and ε estimated from the “spatial spectra” method –
71 a method which involves taking the Fourier transform of a dataset of Doppler velocity measurements
72 sampled either along a single ray at a given time, or at a fixed range gate over a period of time.
73 Bouniol *et al.* (2003) performed a similar evaluation of the Doppler variance method using the spatial
74 spectra method with a vertically-pointing Doppler cloud radar. Point-for-point comparison of ε from
75 the two methods showed a high level of agreement, especially for larger values. They concluded that
76 the Doppler variance provides a reliable estimate of ε . The spatial spectra method itself has been
77 evaluated by Shupe *et al.* (2012), who analysed Doppler velocity time series sampled with a
78 vertically-pointing cloud radar in stratocumulus clouds. They found ε estimates from spatial spectra
79 to correspond well with aircraft and sonic anemometer measurements. Albrecht *et al.* (2016)
80 examined cloud-top entrainment processes in non-precipitating stratocumulus using vertically-
81 pointing Doppler cloud radar. In this study, estimates of ε were derived using both the Doppler
82 spectrum variance and the Doppler velocity power spectrum (Fang *et al.*, 2014), with good agreement
83 found between the two methods. Methods to retrieve ε at vertical incidence in (precipitating and non-
84 precipitating) stratocumulus using Doppler cloud radar are not well suited to retrieve ε with scanning
85 Doppler weather radar in precipitating convective clouds; as pertains to this study.

86 For scanning Doppler weather radar, the most significant contributor to Doppler variance aside
87 from turbulence is generally shear of the radial wind across the three dimensions of the beam (see
88 Section 5), which requires careful separation from turbulence before estimates of ε can be made.

Observing turbulence in convective clouds

89 Melnikov and Doviak (2009) present a detailed method to retrieve ε from the Doppler spectrum in
90 vertical cross-sections through stratiform precipitation collected using an S-band Doppler weather
91 radar. In their study, the radial and elevation shear components are calculated by least-squares fitting
92 contiguous Doppler velocity measurements separately in each direction. A similar, though more
93 sophisticated technique is applied in Section 5.3 to use linear regression to fit a 2-D linear velocity
94 surface model (Neter and Wasserman, 1974) to Doppler velocities to evaluate shear over a spatial
95 scale that we can specify and fix, guided by estimates of the inertial sub-range outer-scale (see Section
96 5.2). Using this method, we have been able to test the sensitivity of retrieved ε to the scale over which
97 shear is calculated and removed (Section 5.5).

98 Melnikov and Doviak (2009) calculated the azimuthal (transverse) shear from velocity gradients
99 between two adjacent scans separated by 2° . They found variances from azimuthal shear to be small
100 compared to elevation shears in stratiform clouds. However, stronger horizontal shears are likely to
101 be found in the convective clouds analysed in this application; in particular, along the edges of
102 updrafts (e.g. Istok and Doviak, 1986). In the present application, our radar data includes one scan
103 performed through one azimuth per cloud. Consequently, we have developed new methods to
104 estimate the azimuthal shear component from the radial shear alone (Section 5.4), allowing for its
105 variance contribution to be estimated when adjacent scans are not available.

106 Generally, past studies focus on single storm cases when using radar methods to investigate
107 convective storm turbulence (e.g. Brewster and Zrnic, 1986; Istok and Doviak, 1986). Often, the
108 contributions to the Doppler spectrum width from mechanisms aside from turbulence are either
109 purely assumed to be negligible, or are shown to be negligible only for the purpose of the application.
110 As a result, a comprehensive method to retrieve ε from radar fields under a wide range of conditions,
111 and the statistical assessment of ε that such a method permits, have not been presented. In developing
112 this comprehensive approach, comparison is made with the more limited approaches that have
113 appeared in the literature.

Observing turbulence in convective clouds

114 In Sections 2 – 5 of this paper, we present methods to accurately determine ε from radar fields.
115 This includes a summary of the conditions under which certain terms in the Doppler spectrum width
116 equation can be neglected, and detailed methods for their calculation when they cannot. By applying
117 this method across a dataset of radar observations, we have performed a statistical assessment of ε in
118 convective storms; this is presented in Section 6.

119

120 2 Data and Methods

121 2.1 DYMECS – Radar observations with CAMRa

122 This investigation follows on from the Dynamical and Microphysical Evolution of Convective
123 Storms (DYMECS) project (Stein *et al.*, 2014). The primary objective of DYMECS is to apply a
124 statistical approach to investigate the dynamics, morphology and evolution of convective storms over
125 southern England, both in radar observations and in high-resolution Met Office Unified Model
126 (MetUM) simulations. An innovative track-and-scan method was used to obtain radar observations
127 of hundreds of convective storms in 2011-2012. These were collected using the Chilbolton Advanced
128 Meteorological Radar (CAMRa) located at the Chilbolton Observatory in Hampshire, UK. CAMRa
129 is a 3 GHz (S-band) Doppler weather radar with dual-polarisation capability. The 25-m diameter
130 antenna provides an angular beam-width of 0.28° . The narrow beam provides elevation, θ and
131 azimuthal, φ resolutions of 100 m at 20 km range, and 500 m at 100 km range. In the radial direction,
132 the pulse has a length of 75 m, however, this is averaged to 300 m in our observations.

133 Observations were collected by scanning with CAMRa in two modes: elevation scanning with
134 RHIs (range-height indicator) and azimuthal scanning with PPIs (plan-position indicator). By
135 alternating between these two modes, detailed observations of hundreds of convective storms were
136 collected on 40 days between July 2011 and August 2012. These observations have been compared

Observing turbulence in convective clouds

137 with MetUM simulations to characterise storm morphology (Stein *et al.*, 2014) and convective
138 updraft characteristics (Nicol *et al.*, 2015) in model and observations.

139 In Section 6, turbulence retrievals are analysed with corresponding fields of vertical velocity
140 retrieved by Nicol *et al.* (2015) for DYMECS observations made on 20 April 2012 and 25 August
141 2012. These updraft velocities were estimated from the Doppler velocity by vertically integrating
142 local changes in horizontal convergence under the assumption of flow continuity, accounting for the
143 changes in density with height. The use of horizontal convergence to estimate vertical velocity
144 removes the need to consider corrections for hydrometeor fall-speeds. The method required a zero-
145 velocity boundary condition, either at the surface or cloud echo top. A weighted combination of
146 velocity derived under both conditions was developed to minimise the vertical propagation of errors.
147 In using only single-Doppler measurements, the omission of convergence in the direction
148 perpendicular to the scanning plane led to a consistent under-estimation of the vertical velocity. To
149 correct for this under-estimation, the suitable scaling for the vertical velocity was estimated from
150 500-m grid-length simulations of the MetUM for each case. These were made under assumptions that
151 the simulated three-dimensional wind flows were suitably realistic and that the range of observed
152 vertical velocities was represented in the model. The uncertainty in retrieved updraft velocities was
153 estimated through point-for-point comparison of the scaled retrievals with model updrafts. For
154 updraft velocities larger than 1 m s^{-1} (as analysed in this study), a root-mean-square difference of
155 2.5 m s^{-1} was found. It is likely that this uncertainty introduces scatter into the relationships between
156 ε and characteristics of updraft velocity presented in Section 6, resulting in weaker measured
157 correlations than may exist between ε and the true updraft strength.

158

159 2.2 Dissipation rates from CAMRa

160 Doppler weather radar, such as CAMRa, can be used to infer characteristics of atmospheric
161 turbulence from observations of the radial velocity field. The mean Doppler velocity \bar{v} , is the

Observing turbulence in convective clouds

162 reflectivity-weighted average of radial point velocities found within a resolution volume (the volume
 163 of atmosphere observed by a single radar pulse, V_6). The Doppler spectrum variance σ_v^2 , estimated
 164 by CAMRa, is the variance in the velocity of reflectors within V_6 . Therefore, σ_v^2 includes velocity
 165 variance due to the turbulent motion of hydrometeors, among contributions from several other
 166 mechanisms. We assume that σ_v^2 can be decomposed into a sum of statistically independent variance
 167 contributions (Doviak and Zrnica, 1984).

$$168 \quad \sigma_v^2 = \sigma_s^2 + \sigma_t^2 + \sigma_{TV}^2 + \sigma_\alpha^2 + \sigma_o^2 \quad (1)$$

169 Where σ_v^2 has contributions primarily from radial wind shear across the sample volume σ_s^2 ,
 170 turbulence σ_t^2 , the distribution of hydrometeor fall-velocities σ_{TV}^2 , antenna rotation σ_α^2 , and
 171 hydrometeor oscillations σ_o^2 .

172 Using the theoretical framework presented by Frisch and Clifford (1974), we can calculate the
 173 eddy dissipation rate, ε from σ_t^2 . Details of turbulent motion cannot be directly measured from σ_v^2 .
 174 We can only infer σ_t^2 from σ_v^2 by accounting for all other variance contributions in (1), either by
 175 subtracting their variance from σ_v^2 , or by demonstrating that they are negligibly small compared to
 176 σ_t^2 .

177 The eddy dissipation rate is the rate of energy transfer through the inertial sub-range of isotropic
 178 turbulence. For calculations of ε to be accurate, σ_t^2 must consist only of velocity variance due to
 179 eddies with a spatial scale less than the largest scale of the inertial sub-range, Λ_0 . Ensuring this
 180 involves the careful separation of shear and turbulence, which is summarised in Section 5.

181 Once σ_t^2 has been determined, ε can be estimated from,

$$182 \quad \varepsilon \approx \frac{1}{\alpha} \left[\frac{\sigma_t^2}{1.35A \left(1 - \frac{\gamma^2}{15}\right)} \right]^{\frac{3}{2}} \quad (2a)$$

Observing turbulence in convective clouds

$$\varepsilon \approx \frac{1}{\beta} \left[\frac{\sigma_t^2}{1.35A \left(1 + \frac{\xi^2}{15}\right)} \right]^{\frac{3}{2}} \quad (2b)$$

184 Where α (in metres) is the angular standard deviation of the two-way Gaussian beam pattern in the
 185 transverse (or elevation) direction (see σ_2 in Appendix S1), multiplied by the range from the radar. β
 186 is the standard deviation of the pulse in the radial dimension (assumed uniform; for CAMRa $\beta =$
 187 26.25m). From this, $\gamma^2 = 1 - \left(\frac{\beta}{\alpha}\right)^2$ and $\xi^2 = 1 - \left(\frac{\alpha}{\beta}\right)^2$, and A is the universal constant of inertial
 188 sub-range turbulence, with a value of 1.6.

189 If $\alpha > \beta$, then (2a) is used, with (2b) to be used if $\alpha < \beta$. This distinction has often been ignored
 190 in past studies, which typically employ a simplified version of (2a) to determine ε (as stated in Doviak
 191 and Zrnic (1984)). For CAMRa, $\alpha > \beta$ at all ranges further than 17.9 km from the radar, so a similar
 192 approximation could be used. However, the application of (2a) and (2b) is straight-forward and any
 193 further approximation should be unnecessary.

194 Values of σ_v^2 generally range from 1 – 25 $\text{m}^2 \text{s}^{-2}$ in our observations. In reality, the negligibility
 195 of terms in (1) depends on their value relative to σ_t^2 , and as a result, no fixed variance value will
 196 always be negligibly small. Assuming that turbulence is only significant when $\sigma_t^2 > 5 \text{m}^2 \text{s}^{-2}$ (this
 197 translates to $\varepsilon > 0.03 \text{m}^2 \text{s}^{-3}$ when $\alpha = \beta$), we choose a negligibility threshold σ_{neg}^2 , of $0.5 \text{m}^2 \text{s}^{-2}$
 198 for the purpose of this application. Whereby, variance contributions that are less than σ_{neg}^2 can be
 199 neglected. We can test the impact of this selection on ε by determining the maximum combined
 200 variance of terms we may neglect. The variance contribution from σ_α^2 is small enough to be ignored
 201 completely ($\sigma_\alpha^2 < 0.01 \text{m}^2 \text{s}^{-2}$, see Section 4). We can calculate σ_s^2 directly (Section 5), so no
 202 element of this contribution is neglected, regardless of value compared to σ_{neg}^2 . However,
 203 contributions from σ_{TV}^2 and σ_o^2 are not simple to measure directly in our observations. Contributions
 204 from σ_{TV}^2 can be larger than σ_{neg}^2 for rain and hail (Section 3), while σ_o^2 is generally less than
 205 $0.25 \text{m}^2 \text{s}^{-2}$ (Section 4). A maximum error would be incurred in σ_t^2 of $0.75 \text{m}^2 \text{s}^{-2}$ when neglecting

Observing turbulence in convective clouds

206 σ_{TV}^2 at $0.5 \text{ m}^2 \text{ s}^{-2}$ (in the extreme case that hail or heavy rain is observed very close to the radar) and
207 σ_o^2 at $0.25 \text{ m}^2 \text{ s}^{-2}$. If $\sigma_t^2 = 5 \text{ m}^2 \text{ s}^{-2}$, this would translate to a 21.6% positive error in ε . The error
208 decreases as turbulence becomes more significant, to only 4.5% when $\sigma_t^2 = 25 \text{ m}^2 \text{ s}^{-2}$, and is
209 independent of the range of the σ_t^2 observation.

210 The range of ε values we can estimate using the Doppler spectrum width technique is determined
211 from the range of σ_v^2 values we can observe. This is related to the maximum ambiguous velocity
212 interval (Nyquist velocity) of the radar. Keeler and Passarelli (1990) state that reliable measurements
213 of the Doppler spectrum width can only be made between 0.02 – 0.2 of the Nyquist interval. CAMRa
214 has a Nyquist interval of 30 m s^{-1} , so we can only reliably observe σ_v between $0.6 - 6 \text{ m s}^{-1}$,
215 corresponding to σ_v^2 of $0.36 - 36 \text{ m}^2 \text{ s}^{-2}$. In the case where $\sigma_t^2 = \sigma_v^2$, we can determine the maximum
216 detectable range in ε from using this method with CAMRa. If observing such a range in σ_t^2 at a range
217 of 50 km, (the typical range of our storm observations), this would correspond to a maximum
218 detectable range in ε of $10^{-3} - 1 \text{ m}^2 \text{ s}^{-2}$.

219 The following three sections outline methods to assess the contribution of the non-turbulent terms
220 in (1). By either calculating these terms directly, or showing that they are negligibly small compared
221 to σ_t^2 , we can remove them from σ_v^2 . This allows us to find σ_t^2 as a residual velocity variance, and
222 then convert this to ε using (2a) and (2b).

223

224 **3 Doppler variance due to a distribution of hydrometeor fall velocities, σ_{TV}^2**

225 *3.1 Theoretical framework and derivation of spectral variance equations*

226 In a given sample volume V_6 , the presence of a distribution of hydrometeor diameters will lead to
227 a distribution of hydrometeor fall velocities. In the circumstance where the radar beam is not
228 perpendicular to hydrometeor velocity, this broadens the Doppler velocity spectrum. The observed
229 variance contribution, σ_{TV}^2 in (1), is at its maximum for a vertically pointing radar beam and decreases

Observing turbulence in convective clouds

230 with angle from zenith. Values of σ_v^2 include the total variance of hydrometeor velocity within the
231 pulse volume. According to (1), the variance in hydrometeor velocity from a fall-speed distribution
232 (σ_{TV}^2) is statistically independent from the variance in hydrometeor velocity resulting from air
233 motions within the cloud (included in σ_s^2 and σ_t^2). Consequently, we require no assumptions
234 regarding the vertical motion of air within the cloud when estimating σ_{TV}^2 .

235 Previous studies to estimate turbulence characteristics from Doppler velocity spectra typically
236 assume σ_{TV}^2 to be negligible (e.g. Frisch and Clifford, 1974; Chapman and Browning, 2001;
237 Meischner *et al.*, 2001; Melnikov and Doviak (2009)) unless observations were made at vertical
238 incidence (Brewster and Zrnic, 1986). The expected variance due to σ_{TV}^2 is reduced significantly by
239 scanning at lower elevations (often the reason σ_{TV}^2 is assumed negligible), however, this does not
240 ensure the contribution is always negligibly small. Melnikov and Doviak (2009) neglected variance
241 contributions from σ_{TV}^2 purely by assuming they remained below $0.2 \text{ m}^2 \text{ s}^{-2}$ when scanning at
242 elevations below 20° through stratiform precipitation. However, results presented in Section 3.2
243 suggest σ_{TV}^2 from raindrops can reach $1 \text{ m}^2 \text{ s}^{-2}$ when scanning at 20° , though this remains dependent
244 on radar reflectivity. The objectives of this section are to: provide a means to estimate σ_{TV}^2 when
245 required, provide justification when neglecting σ_{TV}^2 contributions (showing that $\sigma_{TV}^2 < \sigma_{neg}^2$), and
246 inform how future scanning strategies for turbulence retrieval can be tailored to ensure σ_{TV}^2 is always
247 negligible.

248 For application to RHI radar observations, we classify two hydrometeor types based on the height
249 of the 0°C isotherm, $z_{0^\circ\text{C}}$, which is estimated from the location of bright-band radar reflectivity in
250 our observations. Though $z_{0^\circ\text{C}}$ varies for different DYMECS case days, the average height is ~ 1.5
251 km. For simplicity, we assume any reflectivity returned from below this level is due to liquid
252 raindrops, and any reflectivity from above is due to ice aggregates. By making this simple distinction,
253 we can estimate σ_{TV}^2 in all areas of an RHI scanning domain. In addition to aggregates and raindrops,
254 graupel and hail are also important hydrometeor types, especially in convective clouds. We therefore

Observing turbulence in convective clouds

255 extend our analysis to assess the impact of hail, and consider the effects of graupel (treated as low-
 256 density hailstones) in Section 3.3.

257 We assume the reflectivity for a given V_6 is dominated by one hydrometeor type, and that
 258 hydrometeors are falling vertically downwards at terminal velocity relative to the vertical air motions
 259 within the cloud. We assume hailstones are dry and are of solid ice with homogeneous density. For
 260 hydrometeor mass calculations, we assume that both raindrops and hailstones are spherical.

261 To estimate the relative size of σ_{TV}^2 when compared to σ_v^2 , we can characterise σ_{TV}^2 as the variance
 262 of the reflectivity-weighted mean fall velocity in V_6 as,

$$263 \quad \sigma_{TV_j}^2 = \overline{W_j^2} - \bar{W}_j^2, \quad (3)$$

264 where $\sigma_{TV_j}^2$ has units m^2s^{-2} , W is the reflectivity-weighted hydrometeor fall velocity, and j refers
 265 to the hydrometeor type. We estimate $\overline{W_j^2}$ and \bar{W}_j^2 by evaluating the following integrals,

$$266 \quad \overline{W_j^2} = \frac{\int_0^\infty V_j(D)^2 M_j(D)^2 n_j(D) dD}{\int_0^\infty M_j(D)^2 n_j(D) dD}, \quad (4)$$

$$267 \quad \bar{W}_j^2 = \left(\frac{\int_0^\infty V_j(D) M_j(D)^2 n_j(D) dD}{\int_0^\infty M_j(D)^2 n_j(D) dD} \right)^2, \quad (5)$$

268 where $V_j(D)$, $M_j(D)$ and $n_j(D)$ are terminal velocity-diameter, mass-diameter and particle-size
 269 distribution (DSD) relationships for hydrometeor j , respectively, and D is the hydrometeor diameter
 270 in metres.

271 In (4) and (5), we assume that particle reflectivity is proportional to $M_j(D)^2$. We are in the
 272 Rayleigh scattering regime, and hence this is a reasonable assumption for a 3 GHz radar. The integral
 273 $R_j \int_0^\infty M_j(D)^2 n_j(D) dD$ provides the radar reflectivity in $\text{mm}^6 \text{m}^{-3}$. The term R_j is cancelled out in
 274 (4) and (5), but is given by,

Observing turbulence in convective clouds

275

$$R_j = 10^{18} \frac{|K_j|^2}{|K_{\text{water}}|^2} \left(\frac{6}{\pi \rho_j} \right)^2, \quad (6)$$

276

where $|K_j|^2$ and ρ_j are the dielectric factor and density of hydrometeor j .

277

Terminal velocity-diameter relationships are commonly expressed as simple power laws,

278

$$V_j(D) = p_j D^{q_j}, \quad (7)$$

279

where V is the fall velocity and D is the drop diameter. For ice aggregates, D is the melted diameter.

280

Values of p and q for raindrops, ice aggregates and hailstones are taken from Atlas and Ulbricht

281

(1977), Gunn and Marshall (1958) and Cheng and English (1982), respectively. These have been

282

converted into S. I. units (See Table 1).

283

The hydrometeor mass M , as a function of particle diameter D , can be expressed in the form,

284

$$M_j(D) = a_j D^{b_j} \quad (8)$$

285

where M and D are in S. I. units.

286

We assume that the DSD of each hydrometeor class can be approximated by an exponential

287

distribution of form given by Marshall and Palmer (1948).

288

$$n_j(D) = N_{0_j} \exp(-\lambda_j D) \quad (9)$$

289

Where N_{0_j} and λ_j are the intercept ($n_j(D = 0)$) and slope parameters, respectively, for hydrometeor

290

type j . We consider this a suitable approximation; spectral broadening owing to a distribution in fall

291

velocity has been shown to be nearly independent of the precise shape of the size distribution

292

(Lhermitte, 1963).

293

For rain and ice aggregates, values of ρ , $|K|^2$, a , b and N_0 , are sourced from the UK Met Office

Observing turbulence in convective clouds

294 Unified Model microphysics scheme, as summarised in Stein *et al.* (2014) (See Table 1). For hail,
 295 we use an N_0 of $1.2 \times 10^4 \text{ m}^{-4}$ taken from Waldvogel *et al.* (1978). The sensitivity of $\sigma_{\text{TV}j}^2$ to N_{0j}
 296 is discussed in Section 3.3.

297 To evaluate (3), we first substitute (7) – (9) into (4) and (5) using values from Table 1. By using
 298 a gamma function solution for the integrals in (3) we derive expressions for Doppler spectral variance
 299 contribution for the three hydrometeor varieties. At this point, they are functions only of DSD
 300 parameter, λ_j . Stein *et al.* (2014) provide an expression relating λ_j to radar reflectivity, Z_j ,

$$301 \quad \lambda_j = \left(\frac{R_j a_j^2 N_{0j} \Gamma(1 + 2b_j)}{Z_j} \right)^{\frac{1}{1+2b_j}}, \quad (10)$$

302 where Z_j is the radar reflectivity of hydrometeor j and has linear units of $\text{mm}^6 \text{ m}^{-3}$.

303 Substituting (10) into the $\sigma_{\text{TV}j}^2(\lambda_j)$ expressions and simplifying using values from Table 1,
 304 produces spectral variance equations for rain, ice aggregates and hail,

$$305 \quad \sigma_{\text{TVrain}}^2 = 0.62 Z^{0.191} \sin^2 \theta_{\text{el}}, \quad (11)$$

$$306 \quad \sigma_{\text{TVagg}}^2 = 0.029 Z^{0.119} \sin^2 \theta_{\text{el}}, \quad (12)$$

$$307 \quad \sigma_{\text{TVhail}}^2 = 1.7 Z^{0.143} \sin^2 \theta_{\text{el}}, \quad (13)$$

308 Where Z is in $\text{mm}^6 \text{ m}^{-3}$, $\sigma_{\text{TV}j}^2$ has units of $\text{m}^2 \text{ s}^{-2}$ and θ_{el} is the elevation angle of the reflectivity
 309 observation measured from the surface. Together, these expressions can be used to estimate the
 310 Doppler variance contribution due to the distribution of hydrometeor fall speeds in V_6 .

311

312 3.2 Analysis of $\sigma_{\text{TV}j}^2$

313 Reflectivity measurements in our observations with CAMRa are generally no less than -20 dBZ
 314 (the minimum detectable echo at 10 km range), and no more than 60 dBZ. In our application, we

Observing turbulence in convective clouds

315 therefore classify $\sigma_{TV_j}^2(Z_j = -20 \text{ dBZ})$ and $\sigma_{TV_j}^2(Z_j = 60 \text{ dBZ})$ as the minimum and maximum
316 potential variances we encounter from each hydrometeor type.

317 Equations (11) – (13) show that $\sigma_{TV_j}^2$ increases with radar reflectivity and elevation angle of
318 observation. Assuming a vertically pointing radar beam, and given Z_j in the range of -20 dBZ to 60
319 dBZ, $\sigma_{TV_{\text{rain}}}^2$ increases from 0.26 to 8.62 $\text{m}^2 \text{s}^{-2}$, $\sigma_{TV_{\text{agg}}}^2$ from 0.02 to 0.15 $\text{m}^2 \text{s}^{-2}$ and $\sigma_{TV_{\text{hail}}}^2$ from
320 0.90 to 12.53 $\text{m}^2 \text{s}^{-2}$. For DYMECS observations, RHIs scanned at a maximum elevation angle of
321 15° . Figure 1a displays (11) – (13) for a vertically pointing beam (black lines) and for 15° elevation
322 (grey lines). Compared with a vertically pointing beam, if Z_j is sampled at 15° elevation, values of
323 $\sigma_{TV_j}^2$ are respectively reduced by a factor of 14.

324 A maximum $\sigma_{TV_{\text{agg}}}^2$ of 0.15 $\text{m}^2 \text{s}^{-2}$ suggests that the contribution from ice aggregates is always
325 less than σ_{neg}^2 . Assuming that ice aggregates constitute all hydrometeors above $z_{0^\circ\text{C}}$, then σ_{TV}^2 is
326 negligible for all observations made above this level. For rain observations, which we assume are
327 limited to below $z_{0^\circ\text{C}}$, the equivalent maximum of 8.62 $\text{m}^2 \text{s}^{-2}$ is comparably large, and so $\sigma_{TV_{\text{rain}}}^2$
328 cannot always be neglected. Using (11), we see $\sigma_{TV_{\text{rain}}}^2(60 \text{ dBZ}) < \sigma_{\text{neg}}^2$ for all rain observed at $\theta_{\text{el}} <$
329 13.9° .

330 Under the circumstances that: $\sigma_{TV_{\text{agg}}}^2$ is always negligible, $\sigma_{TV_{\text{rain}}}^2$ is negligible when $\theta_{\text{el}} < 13.9^\circ$,
331 $z_{0^\circ\text{C}}$ can be estimated, and hail is not present, we can describe the negligibility of σ_{TV}^2 in terms of a
332 minimum range from the radar, R_{min} . For our application, R_{min} is simply the range from the radar a
333 pulse reaches a height of $z_{0^\circ\text{C}}$ when transmitted at $\theta_{\text{el}} < 13.9^\circ$. In our RHI observations (where
334 $z_{0^\circ\text{C}} \sim 1.5 \text{ km}$), σ_{TV}^2 is negligibly small everywhere at ranges further than 6.1 km from the radar.
335 While σ_{TV}^2 can still be significant due to rain occurring nearer than R_{min} , below $z_{0^\circ\text{C}}$, it remains
336 conditional on both Z_{rain} and θ_{el} . Observations used in this application were rarely made closer than
337 30 km from the radar, and so we neglect σ_{TV}^2 for rain and ice aggregates.

Observing turbulence in convective clouds

338 According to (13), hail can contribute more to σ_v^2 than rain. However, hail is generally a much
339 less common, more localised occurrence than rain. As a result, the detection of hail using retrieved
340 radar parameters (e.g. hail differential reflectivity H_{DR} , Depue *et al.* (2007)) is necessary before (13)
341 can be reliably applied. If observations do indeed include hail, (13) suggests that $\sigma_{TV_{hail}}^2$ (60 dBZ)
342 falls below σ_{neg}^2 for all hail observations made at $\theta_{el} < 11.5^\circ$. Due to the potential for hail presence
343 both above and below $z_{0^\circ C}$, negligibility based on range from radar is not stated. However, as the
344 minimum range of observations was 30 km, hail would need to be observed at 6 km altitude for
345 $\sigma_{TV_{hail}}^2$ to exceed σ_{neg}^2 , which is unlikely to have occurred.

346 Based on our threshold for negligibility σ_{neg}^2 , the estimation of $z_{0^\circ C}$, and under the assumptions
347 made in the derivation of (11) – (13), we can neglect variance contributions from σ_{TV}^2 in our
348 observations. Due to the dependence of (11) – (13) only on Z and θ_{el} , we expect this conclusion to
349 hold true for other scanning weather radars.

350

351 3.3 Sensitivity of $\sigma_{TV_{rain}}^2$ and $\sigma_{TV_{hail}}^2$ to assumptions

352 In this section, we examine the sensitivity of our results to some of the assumptions made in the
353 derivation of (11) and (13). For ice aggregates, no reasonable sensitivity testing has resulted in the
354 factor 3 increase in $\sigma_{TV_{agg}}^2$ required to even conditionally exceed σ_{neg}^2 . As a result, sensitivity tests
355 involving ice aggregates have been omitted from this discussion, and we conclude that $\sigma_{TV_{agg}}^2$ is
356 always negligible.

357 For rain and hail, we expect little uncertainty in the majority of values in Table 1. The first
358 potential source of uncertainty lies with the treatment of hail as dry with the density of solid ice. We
359 compare $\sigma_{TV_{hail}}^2$ when hailstones are dry with the density of solid ice (assumed in (13)), to low-
360 density and melting hailstones. Melting hailstones will possess a thin outer layer of liquid water,
361 appearing to the radar as large raindrops. To simulate this effect, we change the dielectric factor

Observing turbulence in convective clouds

362 $|K_{\text{hail}}|^2$, in (6) from 0.174 to 0.93. Resulting variance contributions are 21% lower than for dry
 363 hailstones for any given reflectivity. Assuming all hailstones below $z_{0^\circ\text{C}}$ have a liquid water layer,
 364 this reduction leads to $\sigma_{\text{TV}_{\text{hail}}}^2(60 \text{ dBZ}) \approx \sigma_{\text{TV}_{\text{rain}}}^2(60 \text{ dBZ})$ below $z_{0^\circ\text{C}}$. For observations made below
 365 $z_{0^\circ\text{C}} = 1.5 \text{ km}$, we find that $\sigma_{\text{TV}}^2 < \sigma_{\text{neg}}^2$ at all ranges further than 6.5 km from the radar, regardless
 366 of hydrometeor type. If we further consider melting hailstones consisting of low-density ice that is
 367 more consistent with graupel ($\rho_{\text{hail}} = 500 \text{ kg m}^{-3}$), this leads to a combined reduction in $\sigma_{\text{TV}_{\text{hail}}}^2$ of
 368 34%, at which point $\sigma_{\text{TV}_{\text{hail}}}^2(60 \text{ dBZ}) < \sigma_{\text{TV}_{\text{rain}}}^2(60 \text{ dBZ})$, and we revert to neglecting σ_{TV}^2 at ranges
 369 further than 6.1 km.

370 A second source of uncertainty lies with the chosen values of N_0 ; respective values for rain and
 371 hail are assumed constant. For rain, we use $N_{0\text{rain}} = 8 \times 10^6 \text{ m}^{-4}$ from Marshall and Palmer
 372 (1948), who demonstrate its independence of rainfall intensity. The assumption of a constant $N_{0\text{hail}}$
 373 is not as safe as for raindrops as it depends on the largest hail diameter, D_{max} , and has been shown
 374 to vary from $10^3 - 10^5 \text{ m}^{-4}$ (Ulbricht, 1974). Our chosen value of $N_{0\text{hail}} = 1.2 \times 10^4 \text{ m}^{-4}$ from
 375 Waldvogel *et al.* (1978) is roughly in the centre of this range, and is very similar to values of $1.1 -$
 376 $1.4 \times 10^4 \text{ m}^{-4}$ presented by Ulbricht (1977). We test the effect of decreasing values of N_0 for rain
 377 and hail by an order of magnitude. This decrease is chosen to be large enough to roughly account for
 378 the maximum potential variability in N_0 . The result is a 55% increase in $\sigma_{\text{TV}_{\text{rain}}}^2$ and a 39% increase
 379 in $\sigma_{\text{TV}_{\text{hail}}}^2$. Such a large increase in $\sigma_{\text{TV}_{\text{rain}}}^2$ is unlikely given the confidence in our selection of $N_{0\text{rain}}$
 380 (Marshall and Palmer, 1948). However, the corresponding increase for $\sigma_{\text{TV}_{\text{hail}}}^2$ is more likely realised
 381 given the stated uncertainty in $N_{0\text{hail}}$. Such an increase would imply that $\sigma_{\text{TV}_{\text{hail}}}^2(60 \text{ dBZ}) < \sigma_{\text{neg}}^2$
 382 only if observed at $\theta_{\text{el}} < 9.8^\circ$. By instead increasing values of N_0 by an order of magnitude (not
 383 shown), we see a reduction in $\sigma_{\text{TV}_{\text{hail}}}^2$ and $\sigma_{\text{TV}_{\text{rain}}}^2$ of 36% and 28%, respectively.

384 A final source of uncertainty lies with the selected velocity-diameter relationship for hail,
 385 $V_{\text{hail}}(D)$. There is a broader diversity in these relationships in the literature than for rain; we assume

Observing turbulence in convective clouds

386 the $V_{\text{rain}}(D)$ power law provided by Atlas and Ulbricht (1977) to be accurate. Figure 1b compares
 387 $\sigma_{\text{TV}_{\text{hail}}}^2$ from (13) derived using $V_{\text{hail}}(D)$ from Cheng and English (1982), Ulbricht (1977), and
 388 Pruppacher and Klett (1978). As the $V_{\text{hail}}(D)$ proposed by Ulbricht (1977) involves the same
 389 exponent ($q = 0.5$) as that used for (13), the resulting effect is a 29% increase in $\sigma_{\text{TV}_{\text{hail}}}^2$ for all
 390 reflectivity owing to the different values of p . The $V_{\text{hail}}(D)$ relationship from Pruppacher and Klett
 391 (1978) however, involves $q = 0.8$. This leads to a change in exponent in (13), causing a decrease in
 392 $\sigma_{\text{TV}_{\text{hail}}}^2$ ($Z < 40$ dBZ) and an increase for $\sigma_{\text{TV}_{\text{hail}}}^2$ ($Z > 40$ dBZ). $\sigma_{\text{TV}_{\text{hail}}}^2$ (60 dBZ) is increased by 43%.
 393 Figure 1b suggests that the selection of $V_{\text{hail}}(D)$ can have a substantial and varied effect on $\sigma_{\text{TV}_{\text{hail}}}^2$
 394 which somewhat limits how precisely we can state the conditions that allow us to neglect $\sigma_{\text{TV}_{\text{hail}}}^2$.

395

396 **4 Spectral variance due to antenna rotation, σ_{α}^2 and hydrometeor oscillations, σ_o^2 .**

397 The movements of the radar antenna while scanning will broaden the Doppler spectrum.
 398 Assuming a constant antenna scan rate α , in rad s^{-1} , the spectral variance contribution due to antenna
 399 rotation is provided by Doviak and Zrnic (1984),

$$400 \quad \sigma_{\alpha}^2 = \left(\frac{\alpha \lambda \cos \theta_{\text{el}} \sqrt{\ln(2)}}{2\pi\theta_1} \right)^2, \quad (14)$$

401 where λ is the wavelength of the radar in metres, θ_{el} is the elevation angle from the surface, and θ_1
 402 is the one-way half-power beam width in radians.

403 For CAMRa, $\lambda = 0.0975$ m and $\theta_1 = 5 \times 10^{-3}$ rad. During DYMECS, RHI and PPI
 404 observations were made using scan speeds of $\alpha_{\text{RHI}} = 7 \times 10^{-3}$ rad s^{-1} and $\alpha_{\text{PPI}} = 35 \times$
 405 10^{-3} rad s^{-1} . The contribution from σ_{α}^2 is largest when scanning horizontally ($\cos(\theta_{\text{el}} = 0) = 1$);
 406 in this case $\sigma_{\alpha}^2 < 0.01$ $\text{m}^2 \text{s}^{-2}$ for both RHI and PPI observations, making a negligible ($\sigma_{\alpha}^2 < \sigma_{\text{neg}}^2$)
 407 contribution to σ_v^2 . Observations collected at non-zero elevations (up to 15° in DYMECS) would

Observing turbulence in convective clouds

408 only reduce the value of σ_α^2 . Equation (14) can be used simply to determine the contribution of σ_α^2
409 for radars with much faster scanning speeds.

410 The oscillation of hydrometeors can contribute to σ_v^2 , and has been speculated in Zrníc and Doviak
411 (1989) to lead to over-estimation of ε . They find that σ_o^2 decreases with rain-rate, and generally does
412 not increase above $0.25 \text{ m}^2 \text{ s}^{-2}$, so we neglect these contributions.

413

414 **5 Spectral broadening due to shear of the radial wind, σ_s^2**

415 *5.1 Spectral variance equations for shear*

416 Since we are justified in neglecting σ_{TV}^2 , σ_α^2 and σ_o^2 in (1) for DYMECS observations, we are left
417 with Doppler variance contributions from shear and turbulence. We can derive the turbulent
418 contribution from,

$$419 \quad \sigma_t^2 = \sigma_v^2 - \sigma_s^2, \quad (15)$$

420 for use in (2a) and (2b) to calculate ε .

421 In (15), σ_s^2 represents the sum of Doppler variance contributions from the shear of the radial wind
422 in the elevation θ , azimuthal (transverse across the beam) φ , and radial r , directions. Similar to σ_v^2 ,
423 σ_s^2 can be decomposed into a sum of statistically independent variance contributions from shear in
424 each direction.

$$425 \quad \sigma_s^2 = \sigma_{s\theta}^2 + \sigma_{s\varphi}^2 + \sigma_{sr}^2 \quad (16)$$

426 Various equations have been used in past literature to calculate $\sigma_{s\theta}^2$ and $\sigma_{s\varphi}^2$ that are not mutually
427 consistent (e.g. Chapman and Browning, 2001). In Appendix S1, we provide a derivation of these
428 equations that produces results in agreement with those stated in Doviak and Zrníc (1984). An
429 expression for σ_{sr}^2 is also taken from Doviak and Zrníc (1984), assuming a rectangular transmitted
430 pulse.

Observing turbulence in convective clouds

$$431 \quad \sigma_{s\theta}^2 = \frac{(|S_\theta| R \theta_1)^2}{16 \ln 2} \quad (17)$$

$$432 \quad \sigma_{s\varphi}^2 = \frac{(|S_\varphi| R \theta_1)^2}{16 \ln 2} \quad (18)$$

$$433 \quad \sigma_{sr}^2 = \left(\frac{0.35 |S_r| c \tau}{2} \right)^2 \quad (19)$$

434 Where R is the radial distance from the radar in metres, c is the speed of light in m s^{-1} , and τ is
 435 the pulse duration in seconds (for CAMRa, $\tau = 0.5 \mu\text{s}$). $|S_\theta|$, $|S_\varphi|$ and $|S_r|$ are shear magnitudes in
 436 s^{-1} , calculated from the mean Doppler velocity field. In (17) – (19), velocity and reflectivity
 437 gradients are assumed to be linear across V_6 . Equations (17) and (18) differ only in the shear involved,
 438 as the beam profiles in the θ and φ dimensions are the same.

439 In application to CAMRa, the variability of $\sigma_{s(\theta,\varphi,r)}^2$ with $|S|$ and R is illustrated in Figure 1c. For
 440 $|S_r|$ in the range of 0 to 0.02 s^{-1} , σ_{sr}^2 increases with $|S_r|^2$ from 0 to $0.28 \text{ m}^2 \text{ s}^{-2}$. As the pulse length
 441 is constant, σ_{sr}^2 does not vary with range. If $|S_r| < 0.027 \text{ s}^{-1}$ then $\sigma_{sr}^2 < \sigma_{\text{neg}}^2$, indicating that for our
 442 observations, σ_{sr}^2 is negligibly small except in cases of extreme shear. However, although σ_{sr}^2 is likely
 443 to be small, our chosen method of calculating shear (Section 5.3) permits direct measurement of $|S_r|$
 444 to be made simply. We therefore include contributions from σ_{sr}^2 in σ_s^2 .

445 At 30 km range, for $|S_{\theta,\varphi}|$ in the range of $0 - 0.02 \text{ s}^{-1}$, $\sigma_{s(\theta,\varphi)}^2$ increases from $0 - 0.75 \text{ m}^2 \text{ s}^{-2}$. At
 446 150 km range, this increase is to $18.7 \text{ m}^2 \text{ s}^{-2}$ when $|S_{\theta,\varphi}|$ is 0.02 s^{-1} . This suggests that, even at the
 447 minimum range of 30 km, if $|S_{\theta,\varphi}| > 0.016 \text{ s}^{-1}$, then $\sigma_{s(\theta,\varphi)}^2$ is always greater than σ_{neg}^2 for our data.
 448 Given that shears of this magnitude are quite possible (especially in the elevation direction), $\sigma_{s(\theta,\varphi)}^2$
 449 will need to be considered for all of our observations. The high resolution of CAMRa means that
 450 radial velocity shear measured over small distances often result in negligible (less than $0.5 \text{ m}^2 \text{ s}^{-2}$)
 451 contributions to σ_v^2 , however, as illustrated, this is not true for shear of sufficient values. To ensure

Observing turbulence in convective clouds

452 accuracy in point-to-point values of ε , and consistency in application across full RHI scans, we
453 measure and remove σ_s^2 at each point in our data. In Section 6.2, we provide and discuss an example
454 retrieval for a shower cloud (Figure 8) in which σ_s^2 exceeds σ_{neg}^2 quite widely and represents a
455 significant proportion of σ_t^2 . This example is used to highlight the potential for significant over-
456 estimation of ε in our cases if shear corrections are neglected.

457 5.2 Separation of shear and turbulence - theory

458 The separation of shear and turbulence is a significant challenge. However, methods to make this
459 distinction are guided by the framework employed to derive ε from σ_v^2 summarised in Section 2.2.
460 The calculation of σ_s^2 is necessary to remove velocity variance contributions to σ_v^2 from outside the
461 range of scales sampled by the radar. The scale over which to calculate shear (hereafter referred to
462 as Λ_s) in (17) – (19), should ideally be equal to the largest scale of the inertial sub-range, Λ_0 .
463 However, Λ_s should be strictly no larger than Λ_0 , otherwise the inclusion in σ_t^2 of variance from
464 outside the inertial sub-range will lead to an over-estimation of ε .

465 Without the means to routinely estimate Λ_0 for each of the convective storm observations
466 collected in DYMECS, we refer to past literature. Past studies have utilised Doppler spatial spectra
467 and aircraft measurements to estimate Λ_0 in individual convective clouds (Battan, 1975; Knupp and
468 Cotton, 1982; Brewster and Zrnica, 1986). They found that Λ_0 can be as large as 1.5 – 3 km. These
469 estimates were made in severe thunderstorms/hailstorms with strong, large-scale circulations. In
470 comparison, the convective storms constituting the DYMECS observations are generally much
471 weaker, limiting how applicable these values are to our cases. We assume Λ_0 scales with the size of
472 the largest eddy-generating mechanisms in a convective cloud, i.e. the main updraft circulation. If
473 this circulation is shallow, we expect Λ_0 to be small as the downscale cascade to isotropic turbulence
474 begins at a smaller eddy scale. As updraft heights on DYMECS case days generally ranged from 3 –
475 8 km (Nicol *et al.*, 2015), we assume $\Lambda_0 \sim 1$ km for this application. Chapman and Browning (2001)
476 found a factor two change in Λ_0 to have very little effect on their resulting values of ε . However, this

Observing turbulence in convective clouds

477 involved assuming a Λ_0 of only 200 m for shallow shear layers, so we test the sensitivity of our
478 retrieved ε to the value of Λ_s , summarised in Section 5.5.

479 480 5.3 Separation of shear and turbulence – linear velocity surface approach

481 The application of methods to distinguish σ_s^2 from σ_t^2 will depend on the relationship between the
482 spatial resolution of the radar and Λ_0 . As long as the largest dimension of V_6 is less than Λ_0 , σ_t^2 can
483 be used to estimate ε (Frisch and Clifford, 1974). As this is generally the case for a radar of CAMRa’s
484 resolution, scanning deep convective clouds, σ_s^2 can then be determined from radial velocity shear
485 calculated over enough contiguous V_6 volumes to constitute a spatial scale of Λ_0 .

486 To evaluate shear over a constant spatial scale in data with polar co-ordinates is not straight-
487 forward. With two-dimensional radar data, the most effective way to achieve this is to use least-
488 squares regression to fit a velocity surface to Doppler velocity data. A suitable framework for this
489 velocity surface is taken from Neter and Wasserman (1974), and has been applied in previous ε -
490 retrieval studies (Istok and Doviak 1986, Meischner *et al.*, 2001). When applied to RHIs, the velocity
491 surface is given by

$$492 \quad V_i = V_0 + S_\theta l_{\theta_i} + S_r l_{r_i} + E_i \quad (20)$$

493 where

$$494 \quad l_{\theta_i} = R_0(\theta_i - \theta_0) \quad ; \quad l_{r_i} = R_i - R_0$$

495 The range from the radar is given by R , θ is the elevation angle in radians, and (θ_0, R_0) is the centre
496 point of the surface. V_i is the radial velocity at the point (θ_i, R_i) , and E_i is the velocity difference
497 between the data and the surface. V_0 is the estimated central point velocity and S_θ and S_r are linear
498 elevation and radial shears, respectively. l_{θ_i} and l_{r_i} are the elevation and radial distances between V_i
499 and V_0 .

Observing turbulence in convective clouds

500 The parameters V_0 , S_θ and S_r are determined from the matrix operation,

$$501 \quad \begin{bmatrix} V_0 \\ S_\theta \\ S_r \end{bmatrix} = \begin{bmatrix} n & \sum l_{\theta_i} & \sum l_{r_i} \\ \sum l_{\theta_i} & \sum l_{\theta_i}^2 & \sum l_{r_i} l_{\theta_i} \\ \sum l_{r_i} & \sum l_{\theta_i} l_{r_i} & \sum l_{r_i}^2 \end{bmatrix}^{-1} \begin{bmatrix} \sum V_i \\ \sum V_i l_{\theta_i} \\ \sum V_i l_{r_i} \end{bmatrix} \quad (21)$$

502 Centred to best approximation on a chosen Doppler velocity point, neighbouring data points are
 503 used to constitute (as closely as is possible) a Λ_s – by – Λ_s grid of data, G . Using velocities from G ,
 504 (21) is used to compute linear shears S_θ and S_r , which are attributed back to the data point at the
 505 centre of G . By completing this process for all points in a scan, we obtain fields of S_θ and S_r ,
 506 calculated over a fixed scale. If $\Lambda_s = \Lambda_0$, S_θ and S_r are representative of large eddies and/or velocity
 507 gradients in the ordered background flow. As a result, they can be used in (17) and (19) to determine
 508 $\sigma_{s\theta}^2$ and σ_{sr}^2 .

509 In applying (20) to our observations, we find that data located less than $\sim \frac{\Lambda_s}{2}$ from the edge of
 510 observed clouds will be lost in surface fitting. The grid G will only be partially filled with data for
 511 those V located on the periphery of reflectivity echoes, meaning (21) cannot be performed. The
 512 degree of data loss therefore increases with the value of Λ_s . As we can only account for σ_s^2 where
 513 shear can be measured, this data loss is imposed on retrieved fields of ε . Consequently, this limits
 514 our ability to investigate values of ε associated with entrainment processes near cloud edges.
 515 However, turbulence associated with entrainment into updrafts can still be retrieved in cases where
 516 updrafts are further than $\sim \frac{\Lambda_s}{2}$ from the edge of the radar echo (e.g. Figure 6c and 6f). Although we
 517 lose peripheral data, we benefit from the removal of noise in low reflectivity areas around cloud
 518 edges, which can develop large values of σ_v^2 . The 300-m range resolution of our observations restricts
 519 values of Λ_s to multiples of 300 m in order to include whole radial cells, and a minimum of 600 m to
 520 include at least two radial cells for the calculation of shear. Under these restrictions, assuming $\Lambda_0 \sim$
 521 1 km, we select $\Lambda_s = 900$ m for our observations.

522

Observing turbulence in convective clouds

523 5.4 Variance from azimuthal shear, $\sigma_{S_\varphi}^2$

524 When RHI or PPI scans are performed, the radial velocity field is observed in two dimensions,
525 the radial direction and the scanning direction. However, these fields include data from three-
526 dimensional sample volumes. In terms of RHIs, Doppler variance from azimuthal shear, $\sigma_{S_\varphi}^2$
527 contributes to σ_v^2 , but we are unable to directly estimate it due to scanning in the elevation direction.
528 Unless an adjacent RHI is performed, separated from the first by an angular distance comparable to
529 the width of the beam, S_φ cannot be determined directly. As shown in Section 5.1, variance
530 contributions from $\sigma_{S_\varphi}^2$ cannot be ignored in our observations. To account for $\sigma_{S_\varphi}^2$ in circumstances
531 where it cannot be measured directly, we investigate statistical relationships between $|S_\varphi|$ and $|S_r|$
532 derived from PPI radar observations.

533 PPI scans were performed alongside RHIs scans on DYMECS case days. Doppler velocity fields
534 from PPI scans can be differentiated in the radial and azimuthal directions to determine fields of $|S_\varphi|$
535 and $|S_r|$. By collecting many co-located pairs of $|S_\varphi|$ and $|S_r|$ from these fields, we attempt to
536 parametrise $|S_\varphi|$ as a function of $|S_r|$. Using the result, $|S_r|$ found in RHIs can be used to estimate
537 $|S_\varphi|$, and its uncertainty, allowing us to account for all components of σ_s^2 in RHI scans.

538 In order for relationships derived between $|S_\varphi|$ and $|S_r|$ to be of most benefit, we must impose
539 they are calculated over a mutual spatial scale, consistent with that used to calculate $|S_\theta|$ and $|S_r|$ in
540 RHIs, i.e. $\Lambda_s = 900$ m. To achieve this, we use a version of (20) tailored to PPI scans, where $S_\theta l_{\theta_i}$
541 replaced by $S_\varphi l_{\varphi_i}$, and l_{φ_i} is the azimuthal distance between V_i and V_0 . By generating $|S_\varphi|$ and $|S_r|$
542 values for all V_6 across many PPIs, we could build a dataset consisting of co-located values of $|S_\varphi|$
543 and $|S_r|$ for statistical assessment.

544 Figure 2 shows the independent distributions of approximately 10^6 values of S_φ and S_r sourced
545 from 31 PPIs taken on 20 April 2012 at varying elevations. S_φ and S_r are both approximately
546 normally distributed. The combined two-dimensional distribution of S_φ and S_r is circular Gaussian,

Observing turbulence in convective clouds

547 approximately centred on $S_r = S_\varphi = 0$. Once the magnitude of the values in the combined
 548 distribution is taken, which is the quantity relevant to σ_s^2 , $|S_r|$ is divided into contiguous intervals of
 549 width $1 \times 10^{-4} \text{ s}^{-1}$. For each of these, we extract the associated dataset of $|S_\varphi|$, and generate its
 550 probability density function (PDF). Figure 3 demonstrates that the resulting PDFs are very well
 551 approximated by the gamma distribution, given for a random variable x , by (22).

$$552 \quad \gamma(x|k, l) = \frac{x^{k-1} e^{-\frac{x}{l}}}{\Gamma(k) l^k} \quad (22)$$

553 Using (22), we can accurately simulate the change in the distribution of $|S_\varphi|$ with $|S_r|$. For each
 554 $|S_r|$ interval, we extract the gamma distribution parameters k (shape) and l (scale) from the
 555 corresponding distribution of $|S_\varphi|$. By numerically fitting functions to relationships between (k, l)
 556 and $|S_r|$, we define k and l in terms of $|S_r|$,

$$557 \quad k = \begin{cases} |S_r|(A_1|S_r| + A_2) + A_3, & \text{if } |S_r| \leq 0.0017 \text{ s}^{-1} \\ B_1|S_r| + B_2, & \text{otherwise} \end{cases} \quad (23)$$

$$558 \quad l = C_1|S_r| + C_2 \quad (24)$$

559 where coefficient values are provided in Table 2. For a given value of $|S_r|$, we use (23) and (24) to
 560 produce a PDF of $|S_\varphi|$, and derive our estimate of $|S_\varphi|$ as the mean of this distribution. For a gamma
 561 distribution, the mean is simply the product of k and l .

562 Figure 4 shows the change in median and inter-quartile range (IQR) percentiles of $|S_\varphi|$ with $|S_r|$.
 563 Distributions of $|S_\varphi|$ get broader with $|S_r|$. As a result, the size of the IQR, which provides a
 564 confidence interval for $|S_\varphi|$, increases with $|S_r|$. The median values of $|S_\varphi|$ increase with $|S_r|$
 565 according to (25) which was obtained by least-squares fitting a quadratic function to the median curve
 566 in Figure 4. Mean values of $|S_\varphi|$ also increase with $|S_r|$, with values approximately 25% larger than
 567 the median.

$$568 \quad |S_\varphi|_{\text{med}} = |S_r|(D_1|S_r| + D_2) + D_3 \quad (25)$$

Observing turbulence in convective clouds

569 where coefficient values are provided in Table 2.

570 Using (23) – (25), $|S_\phi|$, and an estimate of its uncertainty, can be determined from $|S_r|$ alone. $|S_\phi|$
571 is then used in (18) to calculate its variance contribution, $\sigma_{S_\phi}^2$. We can now account for all components
572 of σ_s^2 in (16), subtract σ_s^2 from σ_v^2 to find σ_t^2 using (15), and use σ_t^2 in (2a) and (2b) to determine ε .
573

574 5.5 Sensitivity of ε to Λ_s

575 To perform this sensitivity test, ε is determined in RHI scans of convective clouds using different
576 values of Λ_s in methods to calculate σ_s^2 . We use 44 RHI scans performed on 25 August 2012 which
577 provide 3.5×10^5 comparable data points for each Λ_s applied. For all scans, we retrieve $\varepsilon(\Lambda_s)$ where
578 Λ_s is 600 m, 900 m, 1500 m, 2100 m, and 2700 m. As described in Section 5.3, the degree of
579 peripheral data loss in velocity surface fitting increases with Λ_s . To ensure that we are comparing the
580 same data across different Λ_s , the degree of data loss seen when $\Lambda_s = 2700$ m has been imposed on
581 all other fields of ε for each scan.

582 Figure 5 displays the PDFs of $\varepsilon(\Lambda_s)$ using the combined data from all RHIs. It shows that the
583 distribution of ε is largely insensitive to Λ_s , though there is a small increase in the likelihood of low
584 values of ε (less than $0.01 \text{ m}^2 \text{ s}^{-3}$) with decreased Λ_s . When calculating shear over a smaller Λ_s , the
585 shear magnitude, and therefore σ_s^2 , is likely to be higher. This means we remove more of σ_v^2 due to
586 shear, and subsequently derive a lower ε , with the converse true if Λ_s is large. As the change in PDFs
587 of ε is small in Figure 5, we can make rough estimations of Λ_0 (and therefore Λ_s) in the absence of
588 direction measurements, without incurring large errors in ε .

589

590 6 Dissipation rate statistics in DYMECS observations

591 6.1 DYMECS case studies

Observing turbulence in convective clouds

592 By applying the methods detailed in Section 2 – 5 across many radar scans, we have performed a
593 statistical assessment of ε in convective storms. We use two contrasting DYMECS days in 2012 as
594 case studies; 20 April (hereafter the “shower” case) and 25 August (hereafter “deep convection”
595 case). In the shower case, low pressure was situated on the east coast of the UK. Convective showers
596 initiated over southern England in the late morning hours, and drifted north-eastwards through the
597 day. In the deep convection case, low pressure was situated over the Irish Sea. Convective storms
598 were more intense and widespread across southern England, with thunderstorms widely reported in
599 the afternoon (Hanley *et al.*, 2015). Radar observations were collected using CAMRa in both cases,
600 using a scanning algorithm that prioritised more active convective cells, guided in real time by Met
601 Office network radar observations (Stein *et al.*, 2014). As this scanning strategy involved sequential
602 scans of the same cells, a subset of these observations has been taken to include only independent
603 convective storm RHI observations for analysis. This subset consists of 33 RHIs in the shower case,
604 and 44 RHIs for deep convection, however, owing to the 200-km range of CAMRa, multiple
605 convective storms were often present in single RHI scans. In the shower case, these observations
606 show that convection grew to 6 km in height, with updraft vertical velocities w , typically ranging
607 from 1 – 4 m s⁻¹. In the deep convection case, convection grew to 10 km with typical w ranging
608 from 2 – 8 m s⁻¹ (Nicol *et al.*, 2015).

609

610 6.2 Example ε retrievals for convective showers and deep convection

611 Figures 6 and 7 display examples of retrieved ε for individual convective clouds on the shower
612 and deep convection case days, respectively. These examples have been selected to reflect the typical
613 convective storms observed on each day. Figure 6 depicts a convective shower of 6 km height, with
614 a diffuse updraft region where w is 1 – 3 m s⁻¹ (Figure 6c), with a region of strong divergence
615 present in the Doppler velocity above the updraft (Figure 6b). As shown in Figure 6f, ε typically
616 ranges from 0.01 – 0.08 m² s⁻³ with the largest values found within the vicinity of the main updraft.

Observing turbulence in convective clouds

617 The example of deep convection displayed in Figure 7 has a depth of 10 km, and shows multi-cell
618 characteristics with numerous updraft-downdraft circulations present in Figure 7c. The dominant
619 updraft (~ 34 km from the radar) is narrower and much stronger than for the shower case, with w
620 ranging from $8 - 12 \text{ m s}^{-1}$. Divergence is again apparent in the Doppler velocity towards the upper
621 levels of the cloud (Figure 7b). Figure 7f indicates that turbulence is more intense and widespread
622 than for the shower case, with values of ε typically ranging from $0.03 - 0.3 \text{ m}^2 \text{ s}^{-3}$. These values are
623 again associated with the main updraft, with the most intense turbulence ($\varepsilon > 0.3 \text{ m}^2 \text{ s}^{-3}$) found
624 towards the top of the cloud, above the updraft.

625 In many of the cloud cases that were examined to derive the statistics of ε presented later in this
626 section, values of σ_s^2 were small compared to σ_t^2 and largely remained below σ_{neg}^2 . The retrievals
627 presented in Figures 6 and 7 provide examples of this; values of $\sigma_s^2 > \sigma_{\text{neg}}^2$ were absent in the shower
628 cloud and were restricted to a small cluster of 36 pulse volumes in the deep cloud case. This region
629 is evident in Figure 7e, located from $7.5 - 8$ km in height at an approximate range of $33 - 34$ km.
630 Although σ_s^2 was significant in this region, values remained less than 15% of σ_t^2 suggesting that σ_s^2
631 could have been neglected in these two cloud examples without significantly over-estimating ε .

632 Shear corrections are, however, not negligible for all cloud cases considered, especially for those
633 located further from the radar. According to (17) and (18), variances from azimuthal and elevation
634 shear components increase with range squared. Figure 8 presents the ratio of σ_s^2 to σ_t^2 in an example
635 cloud observed between $90 - 115$ km from the radar on 20 April 2012. Within the region of $\sigma_s^2 >$
636 σ_{neg}^2 (black contour) values of σ_s^2 vary between $30\% - 70\%$ of σ_t^2 . Neglecting σ_s^2 in this region would
637 result in the over-estimation of mean ε by 52%. Given that clouds were commonly observed 100 km
638 (or further) from the radar, Figure 8 provides an example of the requirement to remove σ_s^2 in our data
639 to ensure accurate retrievals of ε .

640 By inspecting many retrievals of ε in convective clouds across two contrasting days of convection,
641 the rest of this section is focused on relating ε to convective storm characteristics in a statistical sense.

Observing turbulence in convective clouds

642

643 *6.3 Vertical distribution of ε in convective clouds*

644 Statistics have been collected for ε in vertical layers of 1-km depth from the subsets of RHI
645 observations described in Section 6.1. Using this approach, we can assess the vertical distribution of
646 ε in convective clouds (where $Z > -20$ dBZ), and see how this differs for showers and deep
647 convection.

648 Figure 9 shows how the median, and 25th, 75th and 95th percentiles of ε change with height in the
649 cloud; 0 – 6 km for showers, 0 – 10 km for deep convection. For showers and deep convection, the
650 95th percentiles of ε (hereafter ε_{95}) from 0 – 1 km are approximately the same, at ~ 0.025 $\text{m}^2 \text{s}^{-3}$.
651 For the shower case, this remains approximately constant with height, varying between 0.02 – 0.03
652 $\text{m}^2 \text{s}^{-3}$ and peaking at a height of 5 km. For deep convection, ε_{95} increases significantly with height,
653 becoming twice as large as for the shower case at 6 km height (0.05 $\text{m}^2 \text{s}^{-3}$), and increasing to 0.1
654 $\text{m}^2 \text{s}^{-3}$ at 10 km height. The median ε is an approximately constant 0.01 $\text{m}^2 \text{s}^{-3}$ throughout the 6-
655 km depth of the shower cases. For the same depth of deep convective cloud, the median is almost
656 identical to the shower case, and then increases from 0.01 – 0.03 $\text{m}^2 \text{s}^{-3}$ from 6 – 10 km.

657 The 25th and 75th percentiles of ε follow a very similar pattern to this, indicating that from 0 – 6
658 km the average intensity of turbulence is very similar for both cases. The reason for this is highlighted
659 by Figure 6f and 7f; turbulence is locally intense, but a large proportion of the cloud area is only
660 weakly turbulent in both cases ($\varepsilon \leq 0.01$ $\text{m}^2 \text{s}^{-3}$). This was often the case throughout observations
661 on both days which serves to explain why the bulk of ε values are so similar. Where the cloud is
662 turbulent however, values of ε are much larger in deep convection with much stronger circulations,
663 which is reflected in the notable difference in ε_{95} between the two cases.

664

665 *6.4 ε in convective updraft regions*

Observing turbulence in convective clouds

666 As we are most interested in the turbulent regions of individual convective clouds, and turbulence
667 in observations tends to be associated with convective updrafts (see Figures 6 and 7), we refine this
668 investigation to ε located only in convective updraft regions.

669 The following method has been selected in part to ensure it can be applied identically to numerical
670 model data in future investigations. To detect coherent updraft regions, a flood-fill algorithm is
671 applied to vertical cross-sections of w (T. Stein, personal communication), to automatically detect
672 contiguous regions with w above specified thresholds, and record their co-ordinates. By taking the
673 four spatial extremes of these co-ordinates, a box is drawn around an updraft – defined as an updraft
674 *region*. Updrafts are often irregular in shape in observations, so this approach includes some data
675 surrounding the updraft in the defined region. As a result, we benefit from including some
676 information about turbulence associated with an updraft, without it having to be co-located with
677 specific values of w .

678 Once updraft regions are defined, they are filtered by width and depth to avoid the inclusion of
679 very small, insignificant updrafts that are detected by the algorithm. For the shower case, we used a
680 minimum threshold w of 1 m s^{-1} , and a minimum depth of 2 km. For the deep convection case, we
681 used a minimum threshold w of 1.5 m s^{-1} , and a minimum depth of 3 km. In both cases, a minimum
682 updraft region width of 1.5 km was imposed. The lower thresholds for w and depth used in the shower
683 case were chosen due to the weaker, shallower updrafts observed on that day. Using this approach,
684 77 updraft regions were detected in the shower case, and 101 regions for deep convection. The co-
685 ordinates of each region can then be super-imposed on fields of ε for analysis.

686 Figure 10 displays scatter plots relating ε_{95} for each updraft region to its (a) 95th percentile of w
687 (hereafter w_{95}), (b) 95th percentile of the magnitude of the horizontal gradient in w , $\left|\frac{dw}{dx}\right|_{95}$, (c) updraft
688 width, and (d) updraft depth. In Figure 10a, we see that ε_{95} has a significant ($p < 10^{-3}$) positive
689 correlation with w_{95} for both showers ($r = 0.425$) and deep convection ($r = 0.594$). Correlations
690 with $\left|\frac{dw}{dx}\right|_{95}$ (Figure 10b) are marginally stronger than with w_{95} ($r = 0.517$ for showers, $r = 0.671$

Observing turbulence in convective clouds

691 for deep convection). This suggests that strong gradients in w are more important in generating
692 turbulence than w alone. Weaker positive correlations exist between ε_{95} and the width and depth of
693 updrafts for both showers ($r = 0.295$ for width, and $r = 0.314$ for depth), and deep convection
694 ($r = 0.309$ for width, and $r = 0.390$ for depth). This indicates that the intensity of turbulence is
695 not highly sensitive to the dimensions of the updraft. The consistency of correlations between the
696 two cases, albeit with a smaller range in variable values for the shower case, suggests that these
697 relationships may not be restricted to individual cases, or days of observation.

698 To produce Figure 11, all ε values in an updraft region are added to a distribution based on w_{95} .
699 By doing this, we can assess how the full distribution of ε changes with w_{95} in the two cloud types,
700 instead of just the largest values. These distributions are displayed in the form of cumulative density
701 functions (CDFs) for every 2 m s^{-1} interval in w_{95} . In both the showers and deep convection, a trend
702 towards a lower probability of small ε , and a higher probability of large ε is seen with w_{95} . In both
703 cases, small values of ε (less than $0.01 \text{ m}^2 \text{ s}^{-3}$) are approximately twice as likely to appear in updrafts
704 with $w_{95} < 4 \text{ m s}^{-1}$, than for those $w_{95} > 4 \text{ m s}^{-1}$. In the shower case, ε larger than $0.05 \text{ m}^2 \text{ s}^{-3}$
705 has a probability of less than 0.01 in all updraft regions ($w_{95} < 6 \text{ m s}^{-1}$); whereas for the same w_{95}
706 intervals of deep convection the probability is as large as 0.12. This indicates that stronger turbulence
707 is more likely to be found in deep convective clouds than for showers of the same updraft strength.
708 However, we see only a snapshot of information for each convective cloud; turbulent energy will
709 take time to reach dissipation scales, in which time updrafts could have weakened considerably. The
710 probability of large values of ε (more than $0.1 \text{ m}^2 \text{ s}^{-3}$) is 0 for the shower case, but as high as 0.05
711 for deep convection. When w_{95} is $2 - 4 \text{ m s}^{-1}$, the CDFs of ε are very similar for both cases, further
712 indicating that ε may be a function of storm characteristics independent of case, or day of observation.

713

714 7 Summary and Conclusions

Observing turbulence in convective clouds

715 A comprehensive analysis of processes contributing to the width of the Doppler velocity spectrum
716 has been performed, with the objective of developing a rigorous algorithm to estimate turbulence
717 intensity expressed as a dissipation rate.

718 New equations to quantify the spectral broadening effect due to a distribution of hydrometeor fall
719 speeds (σ_{TV}^2) have been presented for ice aggregates, raindrops and hail. We conclude that $\sigma_{TV_{agg}}^2$ is
720 always negligibly small, and $\sigma_{TV_{rain}}^2$ and $\sigma_{TV_{hail}}^2$ are negligible when observing at elevations lower
721 than 13.9° and 11.5° , respectively. We find that σ_{TV}^2 can be larger than $8 \text{ m}^2 \text{ s}^{-2}$ if scanning vertically
722 through heavy rain or hail, and recommend avoiding high-elevation scanning when attempting to
723 retrieve turbulence from the spectrum width.

724 Methods have been presented to remove contributions to σ_v^2 from shear over scales larger than
725 those sampled by the radar. This was achieved by evaluating shear over a constant spatial scale (Λ_s),
726 using linear velocity surface fitting techniques as employed in past studies. Resulting values of ε
727 have been found to be insensitive to Λ_s . To permit the estimation of ε from σ_t^2 , it is of key importance
728 that the largest dimension of V_6 is lower than Λ_0 .

729 To account for spectrum width contributions from shear in the azimuthal direction, we have
730 derived a new equation for the median azimuthal shear as a function of radial shear alone. This can
731 be used to account for 3-D shear broadening in 2-D radar scans, and can be used simply to further
732 improve the accuracy of retrieved ε . After noting incorrect equations for the calculation of σ_s^2 in the
733 literature, we conclude the correct equations are those derived in Appendix S1.

734 By applying the retrieval method across many observations on two contrasting DYMECS case
735 days, we have produced statistics of ε in convective clouds. Turbulence is generally much stronger
736 in deep convective cloud ($0.03 - 0.3 \text{ m}^2 \text{ s}^{-3}$) than in shower cloud ($0.01 - 0.08 \text{ m}^2 \text{ s}^{-3}$). In both
737 cases, the majority of cloud is generally weakly turbulent, with significant turbulence co-located
738 with, but not limited to, areas of shear and buoyancy. Strong turbulence is more widespread towards
739 the top of deep convective cloud, while vertical profiles of turbulence are approximately constant in

Observing turbulence in convective clouds

740 shower cloud. In updraft regions, turbulence is strongly correlated with updraft strength, and there is
741 evidence that gradients in the vertical velocity are more important in generating strong turbulence
742 than the updraft velocity alone. Turbulence is only weakly correlated with the spatial dimensions of
743 updrafts.

744 Our method has sourced, developed, and added to many decades of turbulence retrieval research
745 to form the most comprehensive approach to date. Though we have ultimately applied the method to
746 a specific radar and observational dataset, the considerations made in Sections 2 – 5 are suitably
747 general, forming a reliable framework for turbulence retrieval with other high-resolution radars
748 capable of sampling inertial sub-range turbulence.

749 Following directly from this research, we have collected new observations of convective clouds
750 with CAMRa, under an improved scanning strategy better suited to turbulence retrieval. By
751 performing multiple RHI scans separated by small azimuthal distances across clouds, we aim to
752 investigate the 3-D structures of turbulence in convective storms.

753 We have also used the results of this investigation to evaluate the performance of the
754 Smagorinsky-Lilly sub-grid scheme through direct comparisons with ε in high-resolution NWP
755 simulations of the observed cases. The degree to which our observations can be used more generally
756 to evaluate turbulence characteristics in CPMs (without the need to simulate the observed cases) is
757 not clear. However, at the very least, our observations can provide guidance for the typical
758 characteristics of ε in clouds for comparison with other high-resolution CPM simulations, given that
759 ε can be found as a diagnostic output from the turbulence parametrisation. To ultimately improve the
760 versatility of our results, we aim to extend our observations to more diverse cloud cases to assess the
761 degree to which our statistics are case-dependent.

762

763 **Acknowledgements**

Observing turbulence in convective clouds

764 This research was conducted with funding from the Natural Environment Research Council
765 (NERC) under the SCENARIO programme. Acknowledgements go to Dr. John Nicol in providing
766 vertical velocity retrievals for the case studies investigated, which have been invaluable to the
767 analysis of turbulence in convective clouds. Further thanks go to staff at the Chilbolton Observatory
768 for the technical support with data from CAMRa.

769

770 **Supporting information:**

771 **Appendix S1 – Derivation of spectral variance equations for shear**

772

773

REFERENCES

- 774 Albrecht BA, Fang M, Ghate VP. 2016. Exploring stratocumulus cloud-top entrainment processes
775 and parameterizations by using Doppler cloud radar observations. *J. Atmos. Sci.*, **54**: 729-742.
- 776 Atlas D, Ulbricht CW. 1977. Path- and area-integrated rainfall measurement by microwave
777 attenuation in the 1-3 cm band. *J. Appl. Meteorol.* **16**: 1322–1331.
- 778 Battan LJ. 1975. Doppler radar observations of a hailstorm. *J. Appl. Meteorol.* **14**: 98-108.
- 779 Blyth AM, Cooper AC, Jensen JB. 1988. A study of the source of entrained air in Montana Cumuli.
780 *J. Atmos. Sci.* **45**: 3944-3964.
- 781 Blyth AM. 1993. Entrainment in cumulus clouds. *J. Appl. Meteorol.* **32**: 626-641.
- 782 Bouniol D, Illingworth AJ, Hogan RJ. 2003. Deriving turbulent kinetic energy dissipation rate within
783 clouds using ground based 94 GHz radar. Preprints, 31st Conf. on Radar Meteorology, Seattle,
784 WA, Amer. Meteor. Soc. 192-196.
- 785 Brewster KA, Zrnic DS. 1986. Comparison of eddy dissipation rates from spatial spectra of Doppler
786 velocities and Doppler spectrum widths. *J. Atmos. Oceanic Technol.* **3**: 440-552.

Observing turbulence in convective clouds

- 787 Chapman D, Browning KA. 2001. Measurements of dissipation rate in frontal zones. *Q. J. R.*
788 *Meteorol. Soc.* **127**: 1939-1959.
- 789 Cheng L, English M. 1982. A relationship between hailstone concentration and size. *J. Atmos. Sci.*
790 **40**: 204-213.
- 791 Clark P, Roberts N, Lean H, Ballard SP, Charlton-Perez C. 2016. Convection-permitting models: a
792 step-change in rainfall forecasting. *Meteorol. Appl.* **23**: 165-181.
- 793 Cox GP. 1988. Modelling precipitation in frontal rainbands. *Q. J. R. Meteorol. Soc.* **114**: 115–127.
- 794 Depue TK, Kennedy PC, Rutledge SA. 2007. Performance of the hail differential reflectivity (H_{DR})
795 polarimetric radar hail indicator. *J. Appl. Meteorol. Climatol.* **46**: 1290-1301.
- 796 Doviak RJ, Zrnic DS. 1984. Doppler radar and weather observations. *Academic Press*.
- 797 Falkovich G, Fouxon A, Stepanov MG. 2002. Acceleration of rain initiation by cloud turbulence.
798 *Nature.* **419**: 151-154.
- 799 Fang M, Albrecht BA, Ghate VP, Kollias P. 2014. Turbulence in continental stratocumulus, part II:
800 Eddy dissipation rates and large-eddy coherent structures. *Bound.-Layer Meteor.*, **150**: 361-380.
- 801 Frisch AS, Clifford SF. 1974. A Study of Convection Capped by a Stable Layer Using Doppler Radar
802 and Acoustic Echo Sounders. *J. Atmos. Sci.* **31**: 1622–1628.
- 803 Grover SN, Pruppacher HR. 1985. The effect of vertical turbulent fluctuations in the atmosphere on
804 the collection of aerosol particles by cloud drops. *J. Atmos. Sci.* **42**: 2305-2318.
- 805 Gunn KLS, Marshall RS. 1958. The distribution of size of aggregate snowflakes. *J. Meteorol. Soc.*
806 **80**: 522-545.
- 807 Hanley KE, Plant RS, Stein THM, Hogan RJ, Nicol JC, Lean HW, Halliwell CE, Clark PA. 2015.
808 Mixing length controls on high resolution simulations of convective storms. *Q. J. R. Meteorol.*
809 *Soc.* **141**: 272-284.
- 810 Istok MJ, Doviak RJ. 1986. Analysis of the relation between Doppler spectral width and thunderstorm
811 turbulence. *J. Atmos. Sci.* **43**: 2199-2214.
- 812 Keeler JR, Passarelli RE. 1990. Signal processing for atmospheric radars. *Radar in Meteorology*.

Observing turbulence in convective clouds

- 813 DOI 10.1007/978-1-935704-15-7_21. 199-229.
- 814 Khain AP, Pinsky MB. 1995. Drops' inertia and its contribution to turbulent coalescence in
815 convective clouds: Part 1. Drops' fall in the flow with random horizontal velocity. *J. Atmos. Sci.*
816 **52**: 196-206.
- 817 Knupp KR, Cotton WR. 1982. An intense, quasi-steady thunderstorm over mountainous terrain, part
818 III: Doppler radar observations of the turbulent structure. *J. Atmos. Sci.* **39**: 359-368.
- 819 Labitt, M. 1981. Co-ordinated radar and aircraft observations of turbulence. Project Rep. ATC 108,
820 MIT, Lincoln Lab, 39 pp.
- 821 Lhermitte RM. 1963. Motions of scatterers and the variance of the mean intensity of weather radar
822 signals. SRRC-RR-63-57. Sperry-Rand Res. Cent., Sudbury, Massachusetts.
- 823 Marshall JS, Palmer WM. 1948. The distribution of raindrops with size. *J. Meteorol.* **5**: 165-166.
- 824 Meishner P, Baumann R, Holler H, Jank T. 2001. Eddy dissipation rates in thunderstorms estimated
825 by Doppler radar in relation to aircraft in-situ measurements. *J. Atmos. Oceanic. Technol.* **18**:
826 1609-1627.
- 827 Melnikov VM, Doviak RJ. 2009. Turbulence and wind shear in layers of large Doppler spectrum
828 width in stratiform precipitation. *J. Atmos. Oceanic Technol.* **26**: 430-443.
- 829 Neter J, Wasserman W. 1974. Applied linear statistical models, 842pp.
- 830 Nicol JC, Hogan RJ, Stein THM, Hanley KE, Clark PA, Halliwell CE, Lean HW, Plant RS. 2015.
831 Convective updraft evaluation in high-resolution NWP simulations using single-Doppler
832 measurements. *Q. J. R. Meteorol. Soc.* **141**: 3177-3189.
- 833 Pinsky MB, Khain AP. 2002. Effects of in-cloud nucleation and turbulence on droplet spectrum
834 formation in cumulus clouds. *Q. J. R. Meteorol. Soc.* **128**: 501-533.
- 835 Pruppacher HR, Klett JD. 1978. Microphysics of clouds and precipitation. D. Reidel Publishers,
836 Dordrecht, 714pp.
- 837 Shupe MD, Brooks IM, Canut G. 2012. Evaluation of turbulent dissipation rate retrievals from
838 Doppler cloud radar. *Atmos. Meas. Tech.* **5**: 1375-1385.

Observing turbulence in convective clouds

- 839 Stein THM, Hogan RJ, Clark PA, Halliwell CE, Hanley KE, Lean HW, Nicol JC, Plant RS. 2015.
840 The DYMECS Project: A statistical approach for the evaluation of convective storms in high-
841 resolution NWP models. *Bull. Amer. Meteor. Soc.* **96**: 939-951.
- 842 Ulbricht CW. 1974. Analysis of Doppler radar spectra of hail. *J. Appl. Meteorol.* **13**: 387-396.
- 843 Vohl O, Mitra SK, Wurzler SC, Pruppacher HR. 1999. A wind tunnel study of the effects of
844 turbulence on the growth of cloud droplets by collision and coalescence. *J. Atmos. Sci.* **56**: 4088-
845 4099.
- 846 Waldvogel A, Schmidt W, Federer B. 1978. The kinetic energy of hailfalls. Part I: Hailstone spectra.
847 *J. Appl. Meteorol.* **17**: 515-520.
- 848 Zrnich DS, Doviak RJ, 1989. Effect of drop oscillations on spectral moments and differential
849 reflectivity measurements. *J. Atmos. Oceanic Technol.* **6**: 532-536.

850

851

852 **Figure Captions**

853

854 **Figure 1.** (a) Change in $\sigma_{TV_j}^2$ for rain, ice aggregates and hail, with radar reflectivity Z_j , and elevation
855 angle, θ_{el} . Black lines refer to observations made at vertical incidence; grey lines at $\theta_{el} = 15^\circ$. (b)
856 The impact on $\sigma_{TV_{hail}}^2$ of using different $V_{hail}(D)$ relationships in the derivation of (13); (1) $p =$
857 142.6 , $q = 0.5$, (2) $p = 162.0$, $q = 0.5$, (3) $p = 359.0$, $q = 0.8$. Results are displayed for $\sigma_{TV_{hail}}^2$
858 sampled at vertical incidence ($\theta_{el} = 90^\circ$). (c) The change in $\sigma_{S\theta}^2$, $\sigma_{S\varphi}^2$ and σ_{SR}^2 (Eq. (17) – (19)) with
859 shear magnitude, $|S|$. Variances $\sigma_{S\theta}^2$, and $\sigma_{S\varphi}^2$ are displayed for ranges 30 km and 150 km, which are
860 roughly the minimum and maximum ranges of radar observations in the DYMECS data. Shears larger
861 than 0.02 s^{-1} were uncommon in our observations. In each panel, the threshold for negligibility σ_{neg}^2 ,
862 is plotted for reference as a dashed line at $0.5 \text{ m}^2\text{s}^{-2}$.

863

Observing turbulence in convective clouds

864 **Figure 2.** Independent distributions of 1×10^6 values of S_φ and S_r sourced from 31 PPI scans
865 performed on 20 April 2012.

866

867 **Figure 3.** Change in the PDFs of observed $|S_\varphi|$ for three selected intervals of $|S_r|$ (solid lines).
868 Distributions of $|S_\varphi|$ are well approximated by Gamma PDFs (22) (dashed lines). The width of each
869 $|S_r|$ interval is $1 \times 10^{-4} \text{ s}^{-1}$, and the interval of $|S_r|$ for each distribution is displayed in the figure
870 titles.

871

872 **Figure 4.** The change in the median, 25th and 75th percentile values of $|S_\varphi|$ with $|S_r|$.

873

874 **Figure 5.** The insensitivity of distributions of ε to the scale Λ_s , over which shear is calculated for
875 σ_s^2 .

876

877 **Figure 6.** Example ε retrieval for an RHI scan of a convective storm performed on the 20 April
878 2012 (showers). Included is (a) radar reflectivity, (b) Doppler velocity, (c) vertical velocity, (d) total
879 Doppler variance, (e) Doppler variance due to shear, and (f) eddy dissipation rate displayed in \log_{10}
880 units. The grey contour outlines reflectivity returns of -20 dBZ.

881

882 **Figure 7.** Equivalent to Figure 6, an example retrieval of ε for an RHI scan of a convective storm
883 performed on the 25 August 2012 (deep convection).

884

885 **Figure 8.** The ratio of shear (σ_s^2) and turbulent (σ_t^2) contributions to Doppler variance in an example
886 shower cloud observed on 20 April 2012. The location of values of σ_s^2 that exceed σ_{neg}^2 is indicated
887 by the black contour. In this example, neglecting σ_s^2 in the contoured region results in the
888 considerable over-estimation of mean ε by 52%.

Observing turbulence in convective clouds

889

890 **Figure 9.** Comparison of the vertical distribution of various percentiles of ε in convective clouds
891 ($Z > -20$ dBZ) on 20 April (showers) and 25 August (deep convection), 2012. Percentiles for each
892 1 km layer are plotted at the midpoint of that layer.

893

894 **Figure 10.** Scatter plots comparing the 95th percentile of ε for each updraft region ε_{95} , on 20 April
895 (showers) and 25 August (deep convection), 2012, to the following corresponding statistics: (a) the
896 95th percentile of vertical velocity w_{95} , (b) the 95th percentile of the magnitude of the horizontal
897 gradient in vertical velocity $\left|\frac{dw}{dx}\right|_{95}$, (c) the updraft width, and (d) the updraft depth.

898

899 **Figure 11.** The change in the cumulative density function (CDF) of ε in updraft regions with
900 different 95th percentile values of w (w_{95}) for 20 April 2012 shower updrafts (black lines) and 25
901 August 2012 deep updrafts (grey lines). Values of w_{95} did not exceed 6 m s^{-1} in any shower updraft
902 region. Values of w_{95} smaller than 2 m s^{-1} were not found in any deep updraft region.

903

904

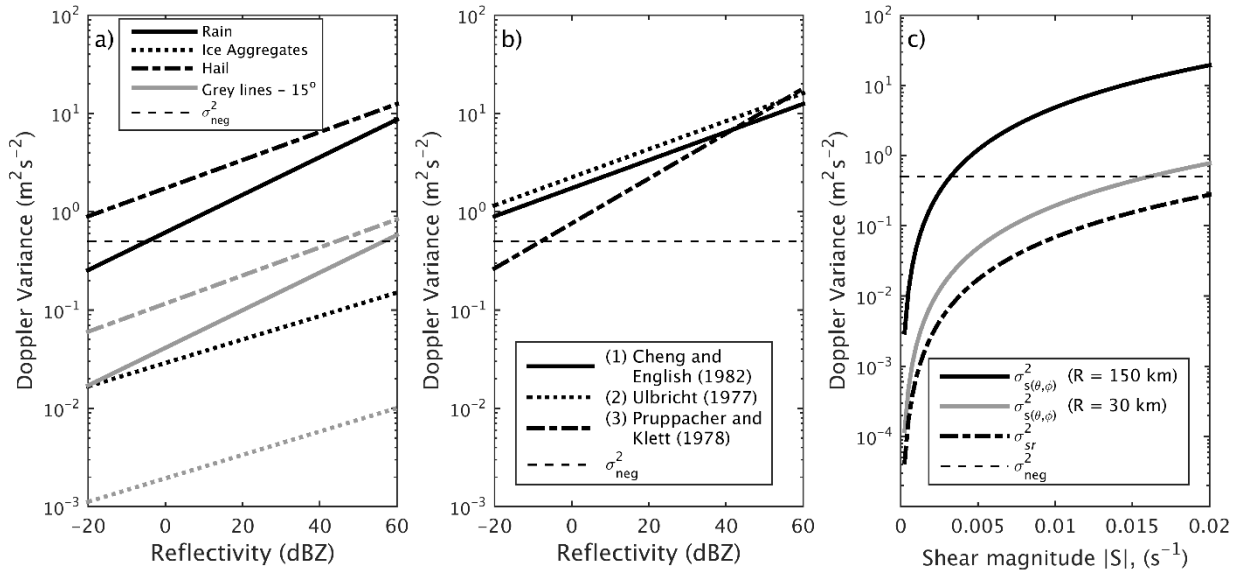
905

906

907

908

909



910

911 **Figure 1**

912

913

914

915

916

917

918

919

920

921

922

923

924

Observing turbulence in convective clouds

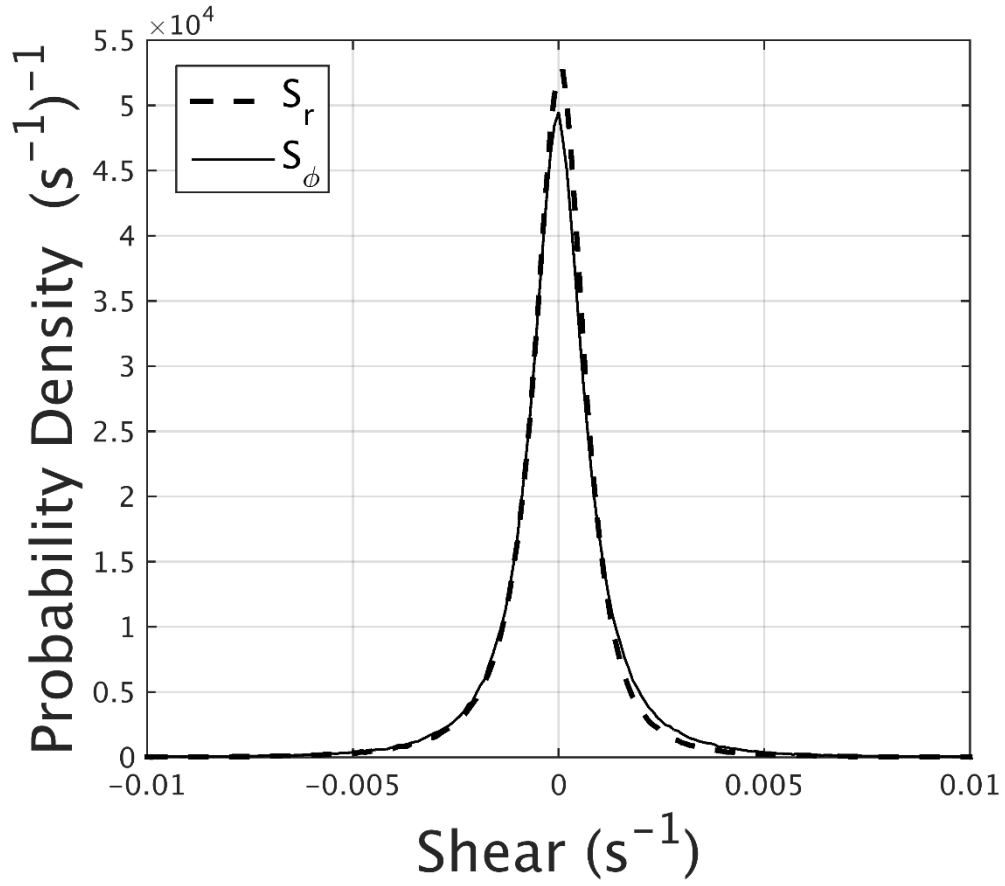
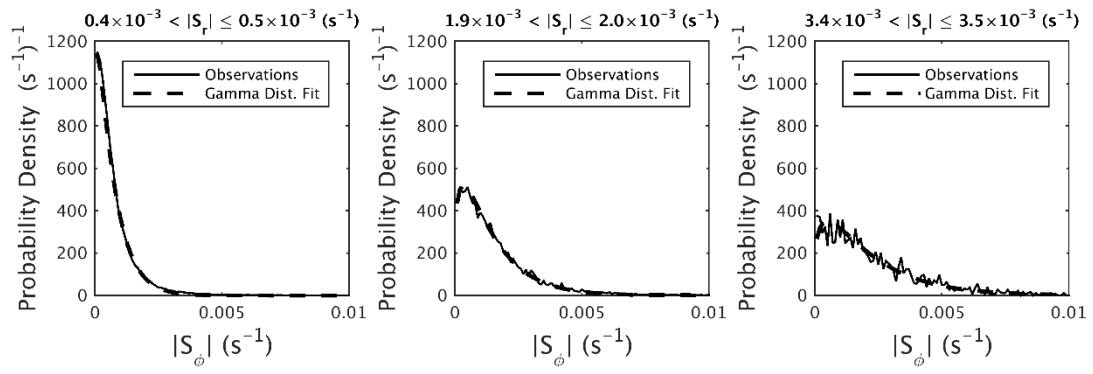


Figure 2

Observing turbulence in convective clouds



956

957 **Figure 3**

958

959

960

961

962

963

964

965

966

967

968

969

970

971

972

973

974

975

976

977

978

Observing turbulence in convective clouds

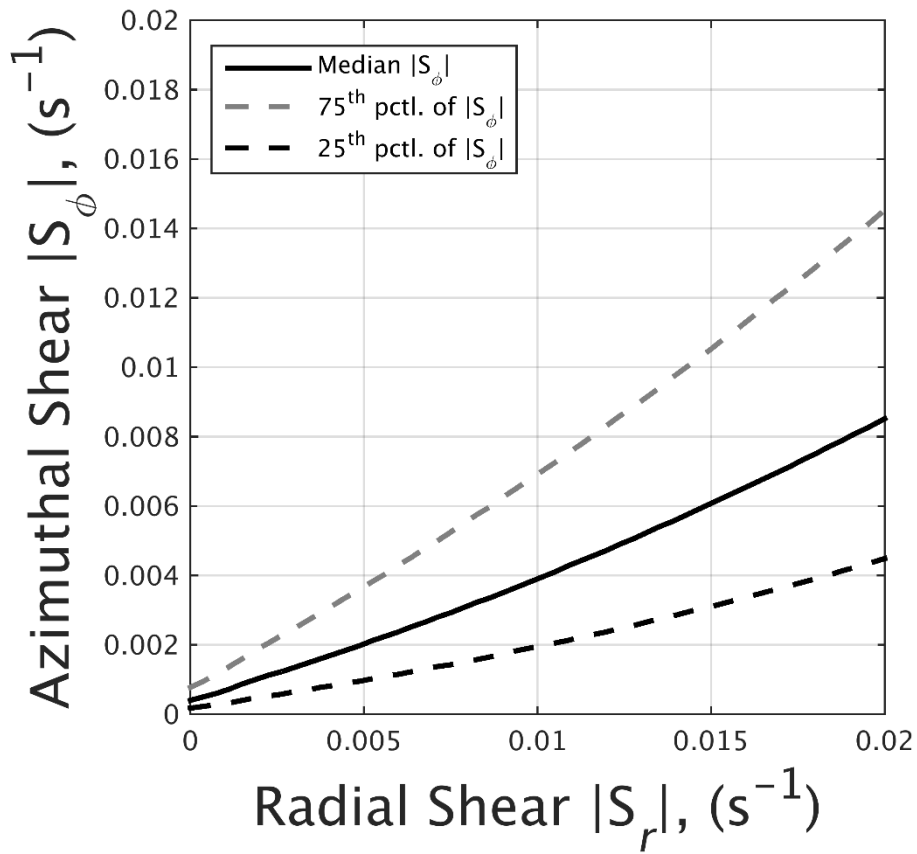


Figure 4

Observing turbulence in convective clouds

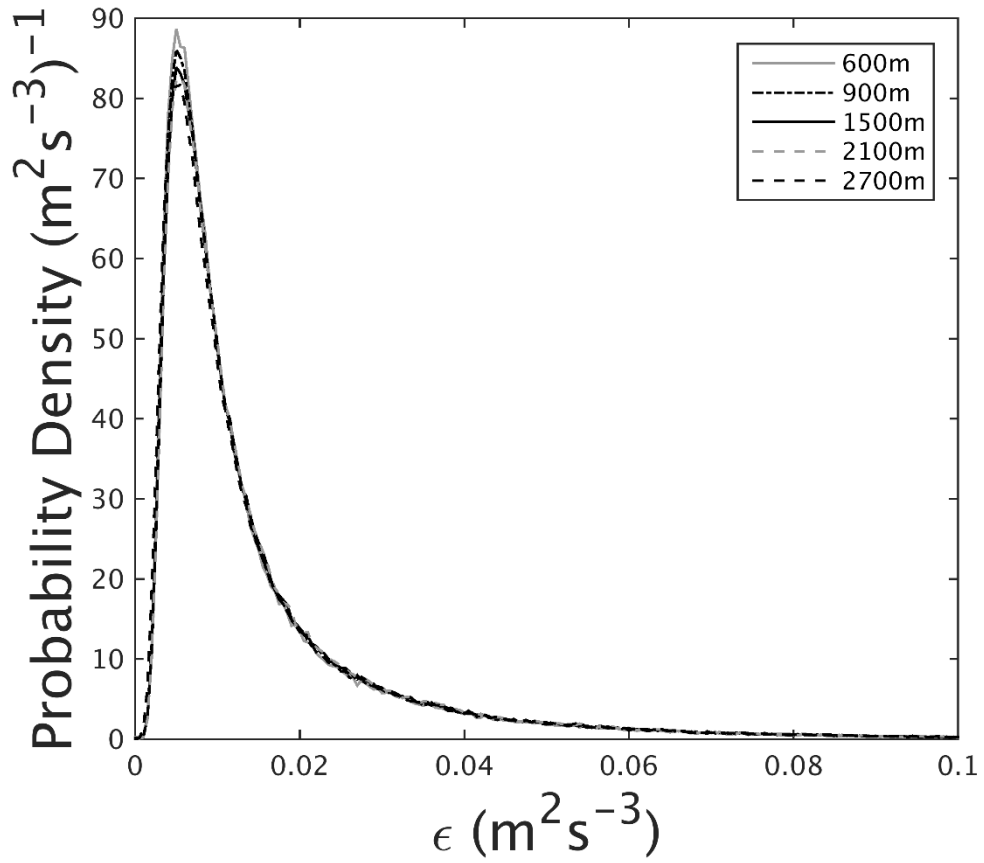
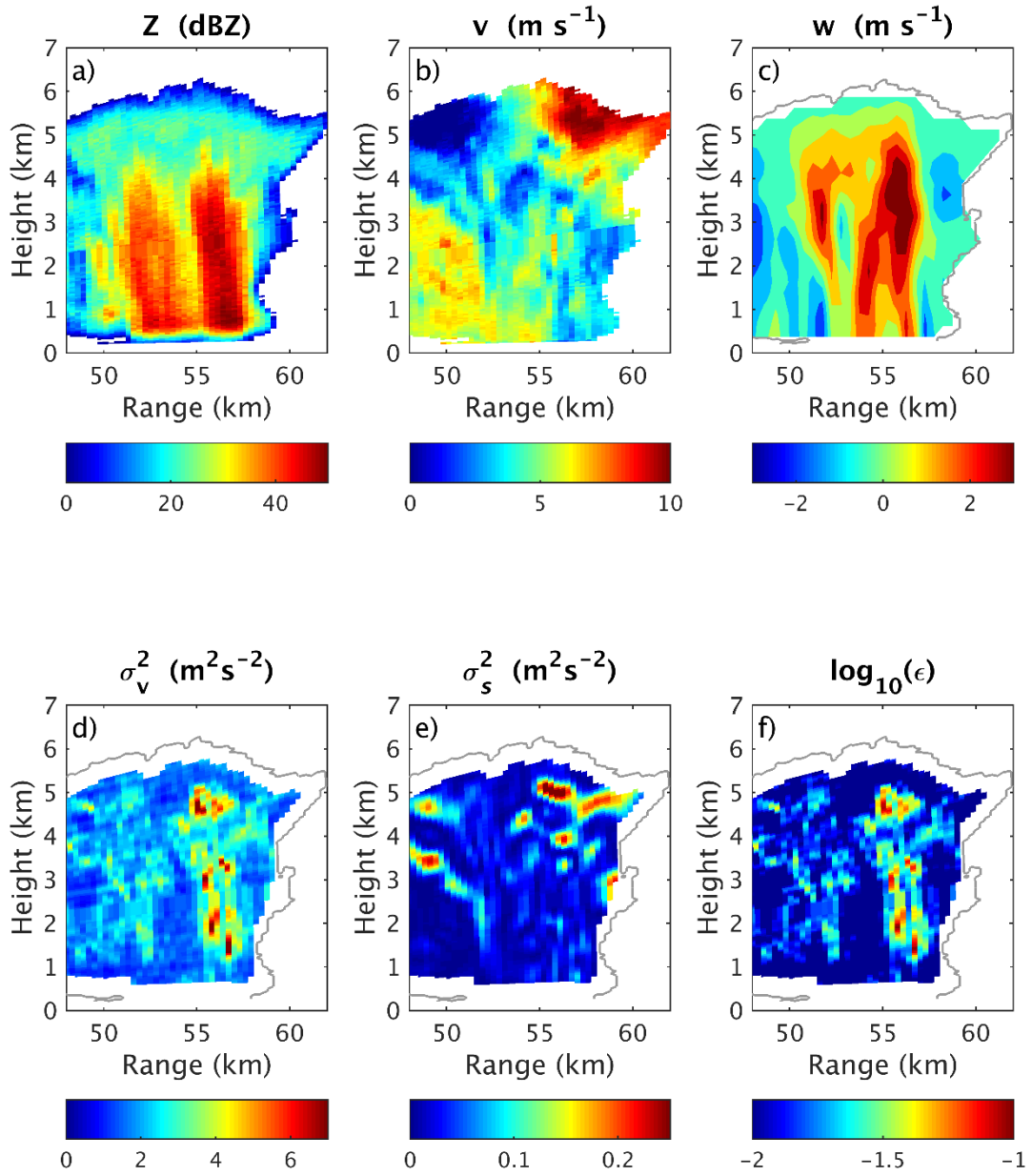


Figure 5

Observing turbulence in convective clouds



1041

1042 **Figure 6**

1043

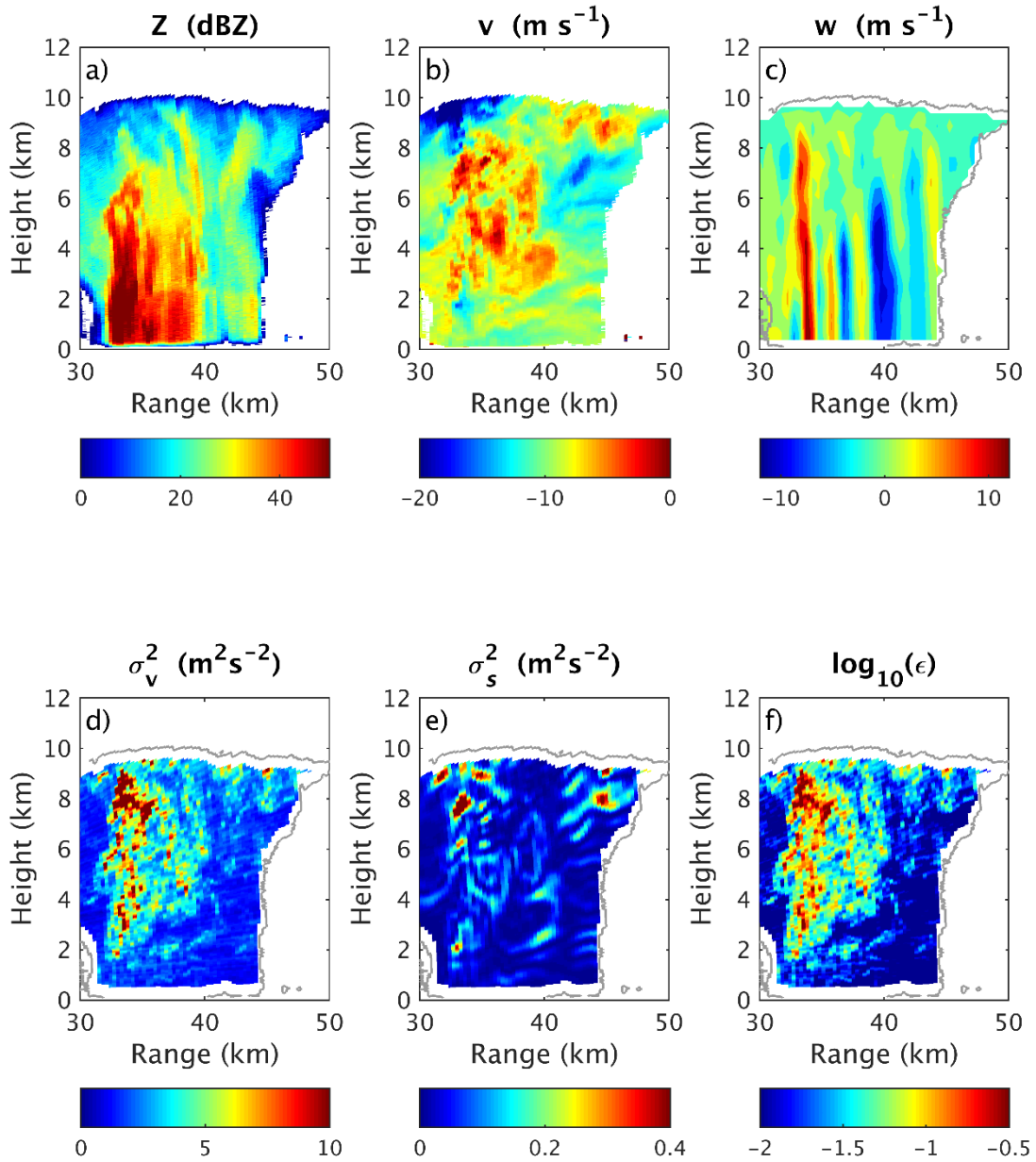
1044

1045

1046

1047

Observing turbulence in convective clouds



1048

1049 **Figure 7**

1050

1051

1052

1053

1054

Observing turbulence in convective clouds

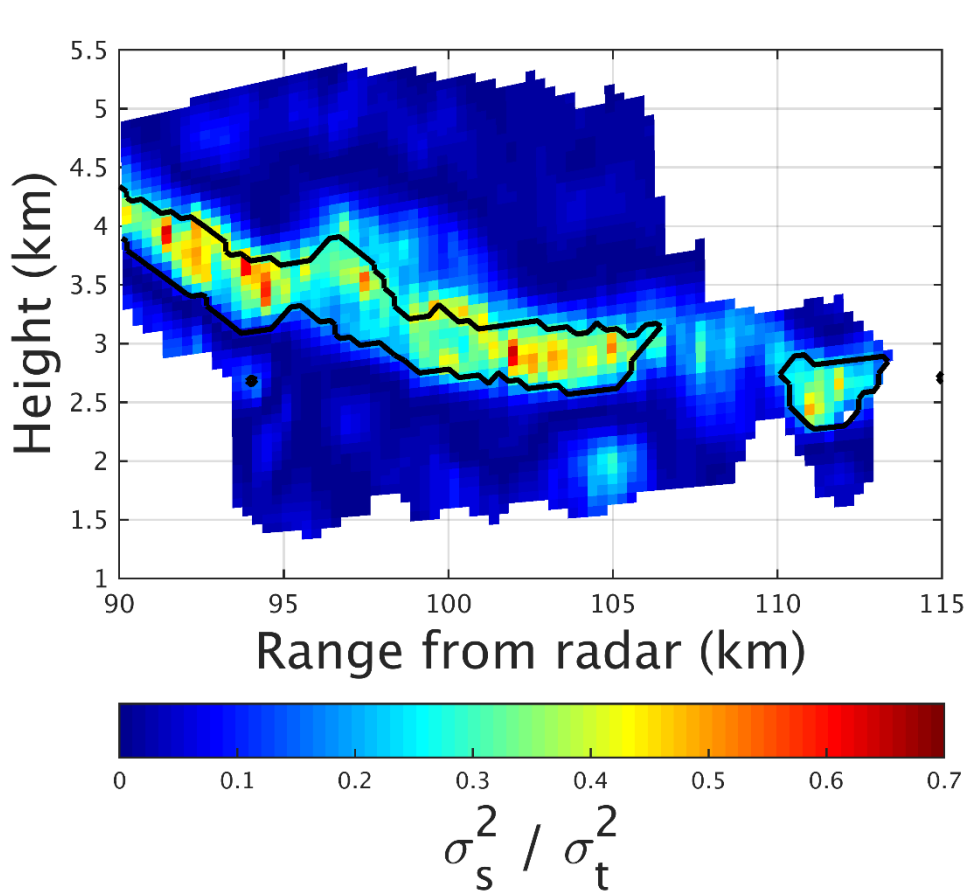


Figure 8

Observing turbulence in convective clouds

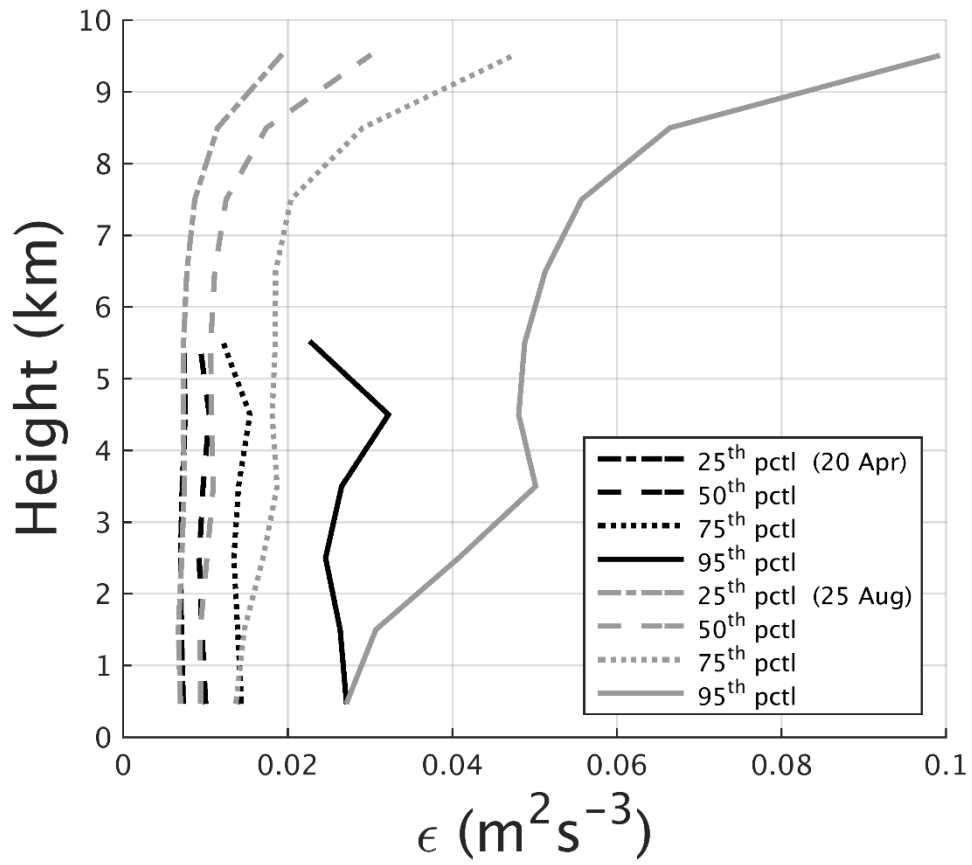
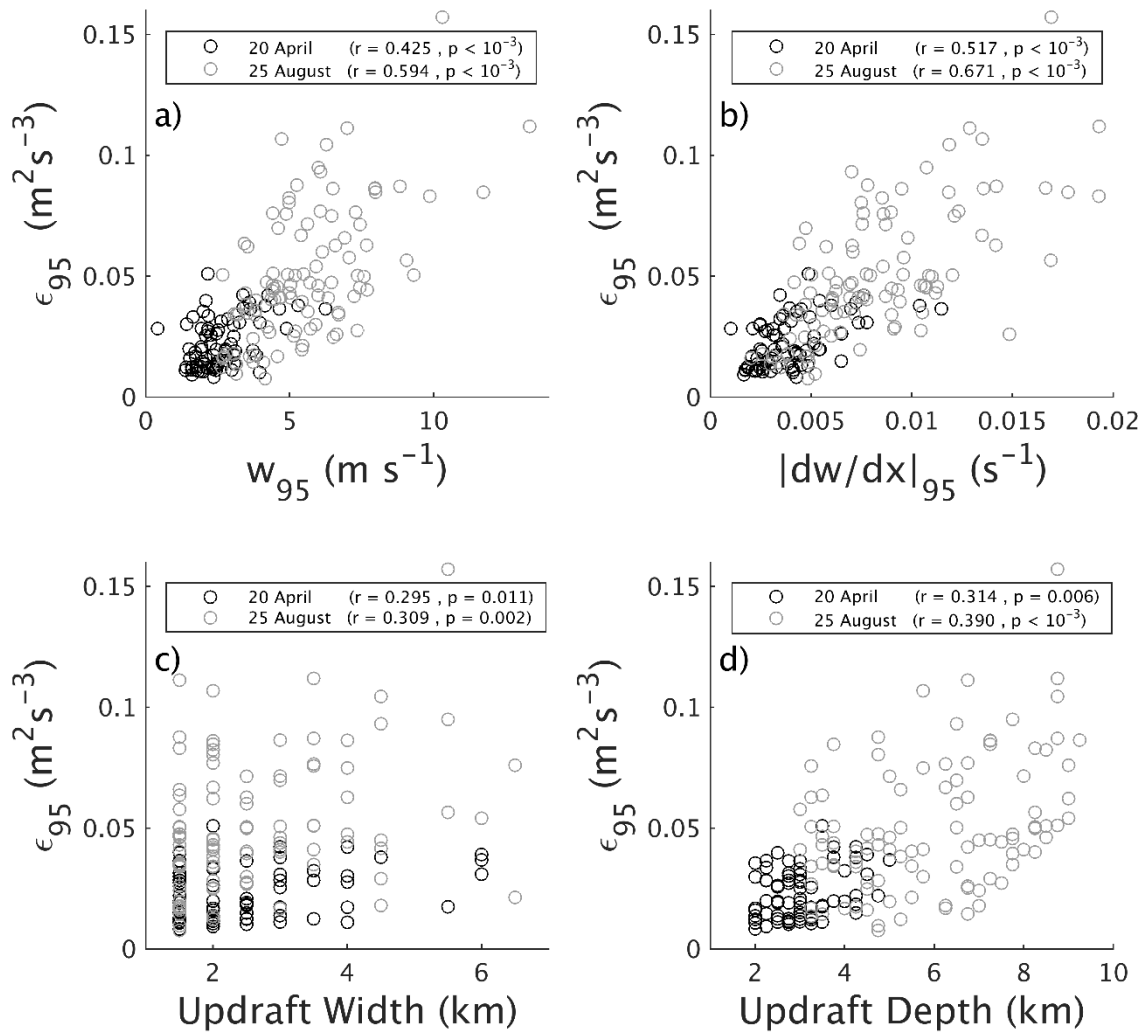


Figure 9

Observing turbulence in convective clouds



1117

1118 **Figure 10**

1119

1120

1121

1122

1123

1124

1125

1126

1127

1128

Observing turbulence in convective clouds

1129
1130
1131
1132
1133
1134
1135
1136
1137
1138
1139
1140
1141
1142
1143
1144
1145

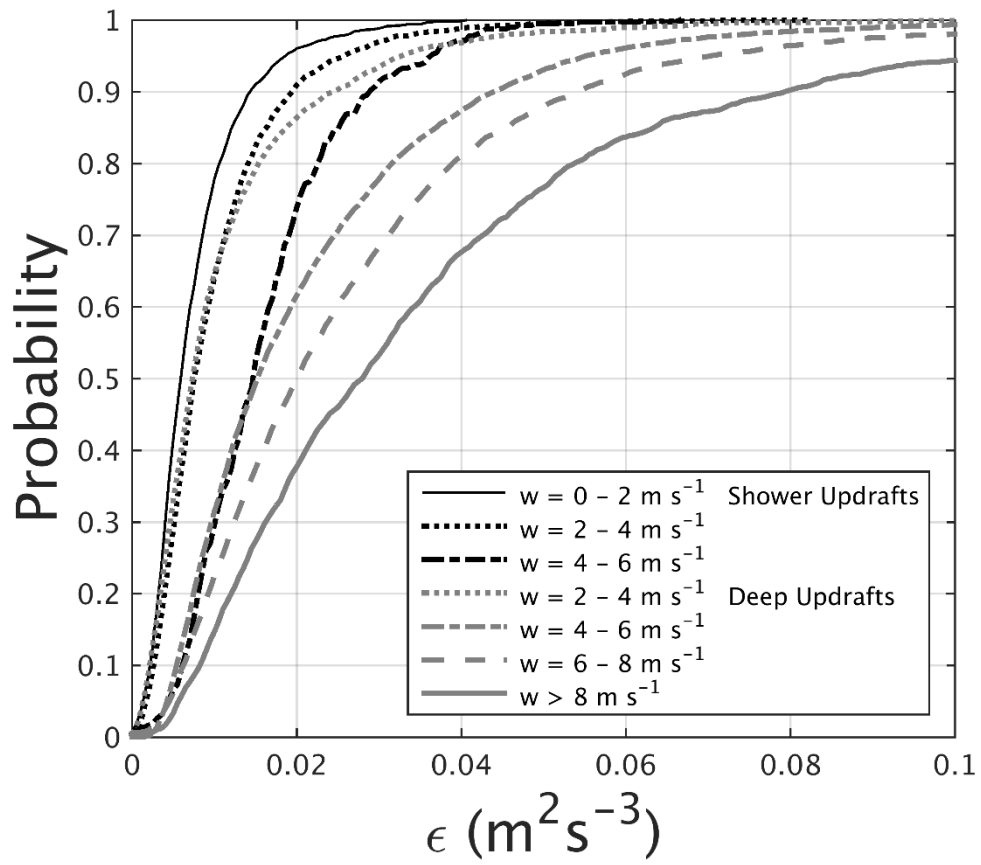


Figure 11